# Study of plasmonic slot waveguides with a nonlinear metamaterial core: semi-analytical and numerical methods



2017 J. Opt. 19 075001

(http://iopscience.iop.org/2040-8986/19/7/075001)

IOP Publishing Journal of Optics
J. Opt. 19 (2017) 075001 (19pp) https://doi.org/10.1088/2040-8986/aa7094

# Study of plasmonic slot waveguides with a nonlinear metamaterial core: semi-analytical and numerical methods

**Mahmoud M R Elsawy and Gilles Renversez**

Aix Marseille Univ, CNRS, Centrale Marseille, Institut Fresnel, 13013 Marseille, France

E-mail: gilles.renversez@univ-amu.fr

Received 6 December 2016, revised 25 April 2017
Accepted for publication 2 May 2017
Published 9 June 2017


**Abstract**

Two distinct models are developed to investigate the transverse magnetic stationary solutions propagating in one-dimensional anisotropic nonlinear plasmonic structures made from a Kerr-type nonlinear metamaterial core embedded between two semi-infinite metal claddings. The first model is semi-analytical, in which we assume that the anisotropic nonlinearity depends only on the transverse component of the electric field and that the nonlinear refractive index modification is small compared to the linear one. This method allows us to derive analytically the field profiles and nonlinear dispersion relations in terms of the Jacobi elliptical functions. The second model is fully numerical and is based on the finite element method in which all the components of the electric field are considered in the Kerr-type nonlinearity, with no presumptions as to the nonlinear refractive index change. Our finite-element-based model is valid beyond the weak nonlinearity regime and generalizes the well-known single-component fixed power algorithm that is usually used. Examples of the main cases are investigated, including those with strong spatial nonlinear effects at low power. Loss issues are reduced through the use of a gain medium in the nonlinear metamaterial core. Using anisotropic nonlinear FDTD simulations, we provide some results for the properties of the main solution.

Keywords: nonlinear waveguides, modelling, finite element method, nonlinear plasmonics, metamaterials, anisotropy, Kerr effect

(Some figures may appear in colour only in the online journal)

## 1. Introduction

Nonlinear optical properties play a crucial role in all-optical integrated circuits due to the different control functionalities they offer [1–3]. Utilizing plasmonics as a part of nonlinear structures may be a promising choice because of the reduced footprint achievable compared with all-dielectric structures, and because of the enhancement of the field intensities, which can be used to boost the nonlinearity [4, 5]. Several nonlinear plasmonic waveguides have already been studied [6–9]. Structures composed of a nonlinear Kerr-type isotropic core sandwiched between two semi-infinite metal claddings have received great attention since their study in 2007 [10], due to the strong light confinement obtained and their peculiar nonlinear effects [11–15]. These nonlinear plasmonic slot waveguides (NPSWs) promise a family of exciting applications such as phase matching in higher harmonic generation processes [16], nonlinear plasmonic couplers [17], or switching [18]. In order to study light propagating in such structures, different methods have been developed [11, 12, 19] to describe its main modes. Recently, a full description of the solutions, including the higher-order ones, was introduced [15, 20]. In addition, an improvement of the NPSWs by the inclusion of two linear dielectric buffer layers between the nonlinear core and the two metal claddings has also been proposed [21, 22]. Nevertheless, all these studies deal only with the standard focusing Kerr-type nonlinear isotropic core. One of the interesting properties of symmetric NPSWs is the existence of the asymmetric mode. This asymmetric mode has no analogue in the linear case, and it

 

bifurcates from the fundamental symmetric mode above a power threshold. This asymmetric mode indicates a strong impact of nonlinearity on the waveguide properties, and is a clear label of a highly nonlinear waveguide. It is worth mentioning that a strong dependence of the dispersion curve on the power is observed before the bifurcation of the asymmetric mode. This mode is the key point for the power-switching operation in nonlinear directional couplers composed of two adjacent NPSWs [17]. The idea behind this application is linked to the change of the state when the power overpasses a certain threshold, i.e. the discrimination of the signals according to their power levels which cannot occur in the low-power regime (before the bifurcation threshold). It appears that the power needed to observe the symmetry-breaking of the fundamental symmetric mode in already-described NPSWs is in the range of GW $m^{-1}$ which is still too high. Otherwise, during the last few years, it was demonstrated that the nonlinear effects can be extremely enhanced using epsilon-near-zero (ENZ) materials [23–27]. However, even if recent experimental results have demonstrated a large enhancement of third-harmonic generation in the ENZ regime [28], the usual modelling approaches are no longer applicable in this high nonlinear regime since the spatial nonlinearity cannot be treated as a perturbation. We have shown in a recent work that, in order to fully take advantage of the ENZ nonlinearity enhancement in nonlinear waveguides, it is important to introduce anisotropy [29]. Even if plasmonic waveguides have already been studied with metamaterial layers either in the cladding [30] or in the core [31, 32], these last studies focused only on the linear guided waves.

In [23], nonlinear guided waves were studied in a one-dimensional multilayer structure in which the layers were set to be parallel to the transverse direction. This means that the dielectric response for the TM polarized waves considered in this multilayer structure is identical to the standard isotropic response, and the metamaterial layers behave like a fully isotropic medium. This alignment of the layers was used to create an ENZ medium and to enhance the nonlinearity. Nevertheless, we have demonstrated in our previous article [29] that, for isotropic nonlinear cores with an ENZ permittivity embedded between two metal cladding, the bifurcation threshold of the asymmetric mode (spatial symmetry breaking induced by the nonlinearity) is not reduced, as it is usually expected from ENZ properties, but increased from the GW $m^{-1}$ to the 100 GW $m^{-1}$ threshold. Moreover, in [29], we have shown that an anisotropic dielectric response can be obtained in the core if the periodic layers are perpendicular to the transverse direction. However, we studied only the influence of the anisotropic linear part of the permittivity on the nonlinear dispersion curves, and the nonlinear permittivity term was assumed to be isotropic and fixed in all the directions. In addition, we neglected the influence of the losses induced by the metamaterial core and by the metal cladding on the nonlinear dispersion curves. In the present work, we consider the same structure as in [29] but consider the full treatment of the anisotropic nonlinear term, i.e. anisotropic linear and nonlinear permittivity tensors, and take into account the losses induced by the metamaterial core and metal claddings. In addition, we provide the full derivation of two distinct methods to study light propagation in a one-dimensional anisotropic structure consisting of a nonlinear metamaterial core with a fully anisotropic dielectric response for the TM polarized waves embedded between two metal claddings. These methods were briefly introduced in [29], while here we present their full derivations. For the first method, which is semi-analytical, this implies both a new classification of the possible cases for the effective nonlinearity and more complicated nonlinear dispersion relations compared with the isotropic case. The second method is based on the finite element method (FEM) and on the fixed power algorithm where the nonlinear stationary solutions are computed numerically as a function of the fixed input power. Usually, it is assumed that only the transverse component of the electric field is taken into account in the nonlinear form. Within this second method, this is not the case since we take into account all the electric field components in the Kerr-type nonlinearity. In order to achieve this result, we introduce and solve two coupled scalar nonlinear equations, one for each continuous tangential component of the electromagnetic field. To the best of our knowledge, this is the first time such a method is used in the frame of the fixed power algorithm.

The validity of the methods and convergence of the FEM are also discussed. Finally, we present two general examples in order to show the influence of the anisotropic linear and nonlinear terms on the nonlinear dispersion curves and on the field profiles compared with the usual NPSWs with an isotropic nonlinear core. The results show that, for one configuration with positive effective nonlinearity, the bifurcation threshold can be reduced by more than three orders of magnitude compared to conventional NPSWs with an isotropic core. This is an indication of a strong enhancement of the spatial nonlinearity. In addition, the losses decrease with the increase in power. This means that we may obtain nonlinear plasmonic solutions at low powers with reduced losses. These interesting results cannot be obtained in conventional NPSWs, in which the losses always increase with the power and the bifurcation threshold is in the range of GW $m^{-1}$. Furthermore, we show that the metamaterial layers can be chosen such that effective nonlinearity has a defocusing behaviour even if we start from a positive Kerr nonlinearity. Once again, this behaviour cannot be observed in isotropic NPSWs. Moreover, we provide some results for the main symmetric mode using nonlinear anisotropic FDTD simulations. The article is organized as follows: in section 2, the statement of the problem is presented. The semi-analytical method and numerical FEM are described in section 3. In section 4, the validation of our models is given by adapting them to study the isotropic case, and a comparison with the results from previously published works is given. In addition, we present several examples to show the influence of the anisotropic nonlinearity on the nonlinear dispersion curves and field profiles. In this section, we also provide results from nonlinear anisotropic FDTD simulations.

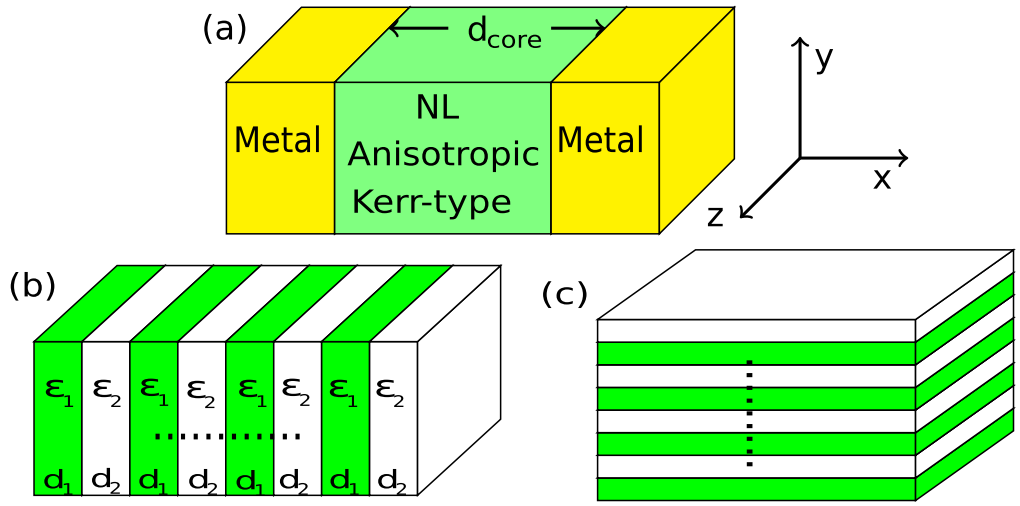


**Figure 1.** (a): Symmetric nonlinear plasmonic slot waveguide geometry with its metamaterial nonlinear core and the two semi-infinite metal claddings. (b), (c) Two different orientations for the nonlinear metamaterial core formed by periodic layers of two different isotropic media.

## 2. Problem formalism

We consider a structured metamaterial nonlinear core, formed by bulk layers, embedded between two semi-infinite isotropic metal claddings (see figure 1(a)). The core layers consist of two different isotropic media with two different permittivities $\epsilon_1$, $\epsilon_2$ and two different thicknesses $d_1$, $d_2$, respectively, as shown in figure 1(b). We propose two different models to study light propagation in such anisotropic nonlinear structures. The first model is based on the approach presented in [15, 20] for isotropic nonlinear core, extending it to structures containing an anisotropic nonlinear core. In this first method, the nonlinearity is treated in an approximated way such that all the components of the permittivity tensor depend only on the transverse component of the electric field. Another limitation is that the nonlinear refractive index change is small compared to the linear refractive index. Based on these assumptions, analytical formulas for the field profiles in terms of the Jacobi elliptical functions [33, 34] are obtained; with the continuity of the tangential electromagnetic field components, they allow us to derive analytical formulas for the nonlinear dispersion relations. This method will be called the extended Jacobi elliptical model (EJEM). Our EJEM is different from the simple model used in references [6, 35], in which only two components of the permittivity tensor depend on the transverse component of the electric field, while in our case we consider the dependence of the transverse component of the electric field for all the components of the permittivity tensor. In addition, the methods used in [6, 35] were developed to study stationary solutions propagating in structures containing a semi-infinite nonlinear region, whereas in our case we consider a finite-size nonlinear anisotropic core. The second model described in the current study is fully numerical and based on the FEM to solve the stationary TM problem in nonlinear layered structures. This numerical FEM does not require any of the assumptions used in the semi-analytical EJEM, and all the components of the effective nonlinear permittivity tensor depend on both the transverse and longitudinal components of the electric field; moreover, the nonlinear term does not need to be small, which means that it is valid beyond the weak nonlinearity regime. In order to treat the nonlinearity in the FEM, we generalize the fixed power algorithm presented in [8, 36] and consider a coupled nonlinear eigenvalue problem to take into account all the electric field components in the Kerr-type nonlinearity instead of the single scalar eigenvalue problem solved previously. Furthermore, in our new model, the nonlinearity is treated without any assumptions relative to its amplitude. It is worth mentioning that the first semi-analytical model (EJEM) provides more insight and understanding into the nature of the stationary solutions in the structure than the second, more numerical model. Nevertheless, the second model treats the nonlinearity in a proper way, without any assumptions on the Kerr-nonlinearity amplitude, but the field profiles are computed numerically.

Our models are written for TM light polarization in which the magnetic field has only one component such that $\boldsymbol{\mathcal{H}} = [0, \mathcal{H}_y, 0]$ and the electric field has two components $\boldsymbol{\mathcal{E}} = [\mathcal{E}_x, 0, \mathrm{i}\mathcal{E}_z]$. We consider only monochromatic TM waves propagating along the $z$ direction in one-dimensional symmetric structures which are invariant along the $z$ and $y$ directions (see figure 1(a)). In these structures, all the field components evolve proportionally to $\exp[\mathrm{i}(k_0 n_{\mathrm{eff}} z - wt)]$: $\boldsymbol{\mathcal{E}}(x, z, t) = \boldsymbol{E}(x)\exp[\mathrm{i}(k_0 n_{\mathrm{eff}} z - wt)]$ and $\boldsymbol{\mathcal{H}}(x, z, t) = \boldsymbol{H}(x)\exp[\mathrm{i}(k_0 n_{\mathrm{eff}} z - wt)]$, where $k_0 = w/c$ represents the wave number in vacuum, $\omega$ denotes the angular frequency of the wave, and $c$ is the speed of light in vacuum. Here $n_{\mathrm{eff}}$ and $k_0 n_{\mathrm{eff}}$ denote the effective index and propagation constant of the wave, respectively. The magnetic field induction vector is defined as $\boldsymbol{\mathcal{B}} = \mu_0 \boldsymbol{\mathcal{H}}$, where the magnetic permeability is constant and is denoted by $\mu_0$, that of vacuum. In our models, we assume that the relative permittivity tensor is complex and diagonal: $\bar{\bar{\epsilon}}(x) = \bar{\epsilon}\,(x) + \mathrm{i}\bar{\epsilon}''(x)$. We consider only the real part of the permittivity $\bar{\epsilon}\,(x) = [\epsilon_x \;\; \epsilon_y \;\; \epsilon_z]$ in the derivation of

the nonlinear dispersion relations, such that the displacement vector is defined as $\boldsymbol{\mathcal{D}} = \epsilon_0 \bar{\bar{\epsilon}} \boldsymbol{\mathcal{E}}$, with $\epsilon_0$ being the vacuum permittivity. The imaginary parts will be used to estimate the losses, in which we use the same method as in [8, 35, 37], extended to the anisotropic case (see section 4). Depending on the chosen orientation of the compound layers relative to the Cartesian coordinate axes, different anisotropic permittivity tensors can be built for the core. Due to the $z$-invariance hypothesis required by our modelling, only two types, where the $z$ axis belongs to the layers, have to be considered. For the first type, where the layers are parallel to the $y$ axis (figure 1(b)), one has for the diagonal terms of $\bar{\bar{\epsilon}}$: $[\varepsilon_x = \varepsilon_\perp\ \varepsilon_y = \varepsilon_{//}\ \varepsilon_z = \varepsilon_{//}]$. For the second case, where the layers are parallel to the $x$-axis, one gets $[\varepsilon_x = \varepsilon_{//}\ \varepsilon_y = \varepsilon_\perp\ \varepsilon_z = \varepsilon_{//}]$ (see figure 1(c)). The first case allows us to obtain an anisotropic effective nonlinear response for TM polarized waves—unlike the second case in which the effective nonlinear response coincides with the standard isotropic one. We will focus on the first orientation of the layers, as depicted in figure 1(b). The nonlinearity considered in this study is the usual Kerr-type, where all the components of the relative permittivity tensor depend on the electric field intensity:

$$\epsilon_j = \epsilon_{jj} + \alpha_{jj}|\boldsymbol{E}(x)|^2 \quad \forall j \in \{x, y, z\}, \tag{1}$$

in which $\epsilon_{jj}$ is the $j$th component of the real linear permittivity tensor and $\alpha_{jj}$ is the corresponding nonlinear parameter, $\forall j \in \{x, y, z\}$. In the metal cladding, $\alpha_{jj} = 0$, and $\epsilon_j = \epsilon_{jj} = \epsilon_m\ \forall j \in \{x, y, z\}$, where $\epsilon_m$ is the real part of the linear metal permittivity. This kind of nonlinearity has already been used in many nonlinear waveguide studies [7, 10, 20, 38], so as a first step we do not need to consider the complex Kerr-type nonlinearity used in [23, 39].

Using the definition of the magnetic field induction $\boldsymbol{\mathcal{B}}$ and displacement vector $\boldsymbol{\mathcal{D}}$, we can express Maxwell's equations for the TM polarized waves as

$$E_x(x) = \frac{n_{\text{eff}} H_y(x)}{\epsilon_0 \epsilon_x(x) c}, \tag{2a}$$

$$E_z(x) = \frac{1}{\epsilon_0 \epsilon_z(x) \omega} \frac{\mathrm{d}H_y(x)}{\mathrm{d}x}, \tag{2b}$$

$$k_0 n_{\text{eff}} E_x(x) - \frac{\mathrm{d}E_z(x)}{\mathrm{d}x} = \omega \mu_0 H_y(x). \tag{2c}$$

Before we describe the derivation of the different methods we will use, we need to explain why we have limited our study to the TM waves. The TE waves in the investigated structures shown in figure 1 have only one null electric field component, the $E_y$ one. Consequently, only the $\varepsilon_y$ component of the permittivity tensor will appear in the TE wave equation. Therefore, the behaviour of these TE waves is identical to the one obtained in the isotropic case. A full study of these waves is provided in our previous work [22] and will not be presented here.

## 3. Derivation of the methods

### 3.1. Extended Jacobi elliptical model (EJEM)

We begin with the derivation of the field profiles and nonlinear dispersion relation in the frame of the EJEM, in which strong assumptions on the form of the Kerr-type nonlinearity are required to establish it. This method is a generalization and an extension of the Jacobi elliptical model (JEM) developed to study the stationary nonlinear solutions in isotropic plasmonic slot waveguides [15, 20], and is based on the same assumptions: (i) the nonlinearity depends only on the transverse component of the electric field and (ii) the nonlinear permittivity modifications are small compared to the linear refractive index such that $\forall j \in \{x, y, z\}$:

$$\epsilon_j = \epsilon_{jj} + \alpha_{jj}|E_x|^2, \quad \alpha_{jj}|E_x|^2 \ll \epsilon_{jj}. \tag{3}$$

These assumptions are valid only at low power, as shown in [7, 8, 20, 38, 40]. However, they allow us to derive analytical formulas for the field profiles inside the anisotropic nonlinear core in terms of the Jacobi elliptical functions [33, 34] which will be used together with the field in the linear metal claddings and continuity of the tangential components at the core/metal interfaces to acquire analytical expressions for the nonlinear dispersion relations.

In order to derive the nonlinear wave equation in terms of the magnetic field component $H_y$ in the frame of the EJEM assumptions, we use equation (2) and proceed as in the isotropic case [8] and find

$$\frac{\mathrm{d}^2 H_y}{\mathrm{d}x^2} - k_0^2 q^2(x) H_y + k_0^2 a_{\text{nl}}^{\text{EJEM}}(x) H_y^3 = 0, \tag{4}$$

where

$$q^2(x) = \begin{cases} q_{\text{core}}^2 = \left( \dfrac{[\Re e(n_{\text{eff}})]^2 \epsilon_{zz}}{\epsilon_{xx}} - \epsilon_{zz} \right) & \text{in the core,} \\ q_m^2 = ([\Re e(n_{\text{eff}})]^2 - \epsilon_m) & \text{in the claddings,} \end{cases} \tag{5}$$

in which $\epsilon_m < 0$ is the real part of the permittivity in the metal claddings. In equation (5), we consider only the real part of the effective index $\Re e(n_{\text{eff}})$ as used in [6, 20, 35]. The nonlinear coefficient $a_{\text{nl}}^{\text{EJEM}}(x)$ is null in the linear metal claddings while, in the nonlinear anisotropic core, it is given by:

$$a_{\text{nl}}^{\text{EJEM}} = \frac{-[\Re e(n_{\text{eff}})]^2}{\epsilon_{xx}^4 c^2 \epsilon_0^2} \times ([\Re e(n_{\text{eff}})]^2 (\alpha_{zz} \epsilon_{xx} - \alpha_{xx} \epsilon_{zz}) - \alpha_{zz} \epsilon_{xx}^2). \tag{6}$$

Our model can be reduced to the isotropic state [8, 15, 20] by setting $\epsilon_{xx} = \epsilon_{zz} = \epsilon_{l,\text{core}}$ and $\alpha_{xx} = \alpha_{zz} = \alpha$ in equations (5) and (6), from which we recover the same expressions for $q^2$ and $a_{\text{nl}}^{\text{EJEM}}$ as in the JEM (the same isotropic response can be obtained with the orientation shown in figure 1(c)). It is worth mentioning that the nonlinear coefficient given by equation (6) is different from what has been developed for the anisotropic case presented in [6, 35]. In these two references

(using our notations to facilitate the comparison), it was assumed that $\epsilon_x$ and $\epsilon_y$ depend on the transverse component of the electric field, while $\epsilon_z$ is assumed not to depend on this component (it is assumed to be constant). In the present study, we consider the dependence of the transverse component of the electric field for all the components of the permittivity tensor. As a special case of the anisotropic treatment, in our recent work [29], we presented the results for an isotropic nonlinear term ($\alpha_{xx} = \alpha_{zz} > 0$) with an anisotropic linear one ($\epsilon_{xx} \neq \epsilon_{zz}$) in order to show the influence of the anisotropic linear part of the permittivity on the nonlinear dispersion diagrams and on the field profiles. In [29], we distinguished between two different cases: the elliptical case, in which $\epsilon_{xx} > 0$ and $\epsilon_{zz} > 0$, and the hyperbolic case, where $\epsilon_{xx} > 0$ and $\epsilon_{zz} < 0$. In the present study, we present a general and full treatment for anisotropic linear and nonlinear permittivity terms with more general classifications based on the sign of $a_{\mathrm{nl}}^{\mathrm{EJEM}}$, which depends on both the effective linear and nonlinear permittivity terms (see equation (6)). In order to solve equation (4), we use the first integral approach [8, 38, 41] and integrate in each of the structure layers separately. Consequently, we can write the nonlinear wave equation as

$$\left(\frac{\mathrm{d}H_y}{\mathrm{d}x}\right)^2 - k_0^2 q^2(x) H_y^2 + k_0^2 \frac{a_{\mathrm{nl}}^{\mathrm{EJEM}}(x)}{2} H_y^4 = C_0, \qquad (7)$$

where $C_0$ is a constant of integration. In the semi-infinite metal cladding, $C_0$ is null since the magnetic field and its derivative tends to zero as $x \to \pm\infty$. Moreover, in the linear cladding, the nonlinear parameter $a_{\mathrm{nl}}^{\mathrm{EJEM}} = 0$ and equation (4) reduces to the standard linear wave equation and the magnetic field matches the usual decaying exponential in the metal regions whose solutions are given by the following (where we add the explicit $x$-dependency on the $H_y$ component):

$$H_y(x) = \begin{cases} H_{\mathrm{left}} \exp\left[k_0 q_m \left(x + \frac{d_{\mathrm{core}}}{2}\right)\right] \text{ for } -\infty \leqslant x < -\frac{d_{\mathrm{core}}}{2}, \\ H_{\mathrm{right}} \exp\left[-k_0 q_m \left(x - \frac{d_{\mathrm{core}}}{2}\right)\right] \text{ for } \frac{d_{\mathrm{core}}}{2} \leqslant x < +\infty. \end{cases} \qquad (8)$$

Here, $H_{\mathrm{left}}$ and $H_{\mathrm{right}}$ are the values of the magnetic field amplitudes at the left $H_y|_{(x=-d_{\mathrm{core}}/2)}$ and the right $H_y|_{(x=+d_{\mathrm{core}}/2)}$ core/metal interfaces, respectively. We are searching for guided wave solutions in the anisotropic waveguides depicted in figure 1, and consequently, we will look only for the solutions with positive attenuation coefficient $q_m$ in the metal claddings (see equation (8)), while the quantity $q_{\mathrm{core}}$ in the core can be either real or imaginary, leading to positive or negative values of $\mathrm{q}_{\mathrm{core}}^2$ (see equation (5)).

In the nonlinear core, $C_0 \neq 0$ and this constant can be obtained in terms of the magnetic field amplitudes at the core/metal interfaces using the continuity of the longitudinal components such that

$$C_0 = k_0^2 H^2_{\left[-\frac{d_{\mathrm{core}}}{2}\right]} \left[\left(\frac{\epsilon_{zz}}{\epsilon_m}\right)^2 q_m^2 - q_{\mathrm{core}}^2 + \frac{a_{\mathrm{nl}}^{\mathrm{EJEM}}}{2} H^2_{\left[-\frac{d_{\mathrm{core}}}{2}\right]}\right]. \qquad (9)$$

A similar expression can be obtained for $C_0$ at the right interface. It is important to mention that the value of $\epsilon_z$ at the left interface is replaced by $\epsilon_{zz}$ in equation (9) since we assumed, in the EJEM, that the nonlinear refractive index change is small compared to the linear one. This expression of $C_0$ is a generalization to those obtained in the isotropic case [20] with different values of $\mathrm{q}_{\mathrm{core}}^2$ and $a_{\mathrm{nl}}^{\mathrm{EJEM}}$, such that we recover the same expression in the isotropic case by setting $\epsilon_{xx} = \epsilon_{zz} = \epsilon_{l,\mathrm{core}}$ and $\alpha_{xx} = \alpha_{zz} = \alpha$ . Due to the anisotropy, the sign of the nonlinear parameter $a_{\mathrm{nl}}^{\mathrm{EJEM}}$ could be positive or negative depending on the values of $\epsilon_{xx}$, $\epsilon_{zz}$, $\alpha_{xx}$, and $\alpha_{zz}$ (see equation (6)). Therefore, we will consider the classification of the nonlinear solutions in the core according to the sign of the nonlinear parameter $a_{\mathrm{nl}}^{\mathrm{EJEM}}$.

*3.1.1. Case $a_{\mathrm{nl}}^{\mathrm{EJEM}} < 0$:* We begin with the case in which $a_{\mathrm{nl}}^{\mathrm{EJEM}} < 0$. In this case, we set $a_{\mathrm{nl}}^{\mathrm{EJEM}} = -|a_{\mathrm{nl}}^{\mathrm{EJEM}}|$ in equation (9) to write the integration constant in the nonlinear core as

$$C_0 = k_0^2 H^2_{\left[-\frac{d_{\mathrm{core}}}{2}\right]} \left[\left(\frac{\epsilon_{zz}}{\epsilon_m}\right)^2 q_m^2 - q_{\mathrm{core}}^2 - \frac{|a_{\mathrm{nl}}^{\mathrm{EJEM}}|}{2} H^2_{\left[-\frac{d_{\mathrm{core}}}{2}\right]}\right]. \qquad (10)$$

Here, we cannot determine directly the sign of $C_0$ according to the sign of $\mathrm{q}_{\mathrm{core}}^2$, and hence the magnetic field component $H_y$ in the core will be classified according to the signs of $\mathrm{q}_{\mathrm{core}}^2$ and $C_0$. Nevertheless, we have found that the only bounded solutions in the nonlinear core in case of a negative value of $a_{\mathrm{nl}}^{\mathrm{EJEM}}$ can be obtained only when $q_{\mathrm{core}}^2 < 0$ and $C_0 > 0$ with the following criterion:

$$q_{\mathrm{core}}^4 \geqslant \frac{2C_0|a_{\mathrm{nl}}^{\mathrm{EJEM}}|}{k_0^2}. \qquad (11)$$

In order to clarify this point, we write equation (7) in the reduced form

$$\frac{\mathrm{d}H_y}{\sqrt{AC_0 - AQH_y^2 + H_y^4}} = \pm\sqrt{\frac{1}{A}}\,\mathrm{d}x, \qquad (12)$$

where the reduced parameters for $q_{\mathrm{core}}^2 < 0$, $a_{nl}^{\mathrm{EJEM}} < 0$, and $C_0 > 0$ are given by

$$A = 2/(k_0^2|a_{\mathrm{nl}}^{\mathrm{EJEM}}|), \qquad Q = k_0^2|q_{\mathrm{core}}^2|. \qquad (13)$$

Now equation (12) can be written as

$$\frac{\mathrm{d}H_y}{\sqrt{(\gamma^2 - H_y^2)(\delta^2 - H_y^2)}} = \pm\sqrt{\frac{1}{A}}\,\mathrm{d}x, \qquad (14)$$

with

$$\gamma^2 = (AQ + \sqrt{(AQ)^2 - 4AC_0})/2, \quad \delta^2 = (AQ - \sqrt{(AQ)^2 - 4AC_0})/2, \qquad (15)$$

where $\gamma^2 > \delta^2$. We are looking for real values of the magnetic field $H_y$, and thus $\gamma^2$ and $\delta^2$ must be real, which means that we need to consider the case $(AQ)^2 \geqslant 4AC_0$; this gives the condition shown in equation (11). In order to ensure that the quantity under the square root in the denominator of the left-hand side of equation (14) is positive, we must consider $H_y^2 < \delta^2 < \gamma^2$. It is worth mentioning that we have found unbounded solutions in the core when the condition in equation (11) is not satisfied (see appendix A for more details). Integrating equation (14) in the nonlinear core and using formula 17.4.45 from [33], we can express the magnetic field profile $H_y$ in the nonlinear core (for $a_{\mathrm{nl}}^{\mathrm{EJEM}} < 0$, $q_{\mathrm{core}}^2 < 0$, and $C_0 > 0$) in terms of the bounded Jacobi elliptical function sn $[u|m]$ with argument $u$ and parameter $m$ [33, 34, 42, 43] as:

$$H_y(x) = \begin{cases} \delta \mathrm{sn}\left[ -\sqrt{\frac{\gamma^2}{A}}\left(x + \frac{d_{\mathrm{core}}}{2}\right) + X_0 \,\middle|\, m \right] & \text{for} \quad \epsilon_{zz} > 0, \\ \delta \mathrm{sn}\left[ +\sqrt{\frac{\gamma^2}{A}}\left(x + \frac{d_{\mathrm{core}}}{2}\right) + X_0 \,\middle|\, m \right] & \text{for} \quad \epsilon_{zz} < 0, \end{cases} \tag{16}$$

where

$$m = \frac{\delta^2}{\gamma^2} \quad \text{and} \quad X_0 = \mathrm{sn}^{-1}\left[ \frac{H_{\mathrm{left}}}{\delta} \,\middle|\, m \right]. \tag{17}$$

Here, $\mathrm{sn}^{-1}[u|m]$ is the inverse Jacobi elliptical function sn $[u|m]$ [33]. In equation (16), the choice of the sign in front of the square roots is related to the sign of $\epsilon_{zz}$ such that, for $\epsilon_{zz} > 0$, we choose the negative sign and for $\epsilon_{zz} < 0$ we choose the positive one. In order to clarify this point, we need to look at equation (12). If the condition given by equation (11) (with $H_y^2 < \delta^2 < \gamma^2$) is satisfied, the expression under the square root in the denominator of the left-hand side of equation (12) is positive, and thus the sign on the right-hand side of this equation only depends on the infinitesimal change of the magnetic field $\mathrm{d}H_y$. In order to be able to study the sign of $\mathrm{d}H_y$ on the numerator of equation (12), we consider the continuity condition of the longitudinal component $E_z$ at the left core/metal interface

$$\frac{k_0 q_m}{\epsilon_m} H_y \bigg|_{x=\left(-\frac{d_{\mathrm{core}}}{2}\right)^-} = \frac{1}{\epsilon_{zz}} \left[ \frac{\mathrm{d}H_y}{\mathrm{d}x} \right]_{x=\left(-\frac{d_{\mathrm{core}}}{2}\right)^+}, \tag{18}$$

in which we substituted $\epsilon_z$ at $x = (-d_{\mathrm{core}}/2)^+$ by $\epsilon_{zz}$ in the frame of the EJEM assumptions. In equation (18), the real part of the permittivity in the metal cladding is negative $\epsilon_m < 0$ (see the text after equation (5)), and we are looking for solutions with positive attenuation coefficient in the metal cladding $q_m > 0$; additionally, without loss of generality, we assume that $H_y|_{(x=-d_{\mathrm{core}}/2)} > 0$. This means that the sign of the magnetic field derivative $[\mathrm{d}H_y/\mathrm{d}x]_{x=(-d_{\mathrm{core}}/2)^+}$ depends on the sign of $\epsilon_{zz}$ such that, for $\epsilon_{zz} < 0$, the sign of the magnetic field derivative is positive, while if $\epsilon_{zz} > 0$, the correct choice of the sign of the magnetic field derivative is the negative one. Therefore, according to the sign of $\epsilon_{zz}$, we choose the sign on the right-hand side of equation (12) and consequently the sign in front of the square roots in equation (16). It is important to notice that, in the isotropic case with positive Kerr nonlinearity, $a_{\mathrm{nl}}^{\mathrm{EJEM}}$ is always positive. Thus, the solutions given by equation (16) for $a_{\mathrm{nl}}^{\mathrm{EJEM}} < 0$ can only be obtained with the anisotropic treatment of the effective nonlinearity presented in this study.

The procedure of the derivation of the nonlinear dispersion relation is similar to what has already been used for the isotropic case [15, 20]: we use the magnetic field profile in the nonlinear core equation (16), the magnetic field in the linear metal claddings (equation (8)), and Maxwell's equations (2). Using the continuity conditions for the tangential electromagnetic field components $H_y$ and $E_z$ at the right core/metal interface ($x = d_{\mathrm{core}}/2$), we can write the nonlinear dispersion relation in terms of the bounded Jacobi elliptical functions sn $[u, m]$, cn $[u, m]$, and dn $[u, m]$ with argument $u$ and parameter $m$ as

$$\begin{aligned} &\frac{-k_0 \epsilon_{zz} q_m}{\epsilon_m} \mathrm{sn}\left[ \pm\sqrt{\frac{\gamma^2}{A}} d_{\mathrm{core}} + X_0 \,\middle|\, m \right] \\ &= \pm\sqrt{\frac{\gamma^2}{A}} \left\{ \mathrm{cn}\left[ \pm\sqrt{\frac{\gamma^2}{A}} d_{\mathrm{core}} + X_0 \,\middle|\, m \right] \right\} \\ &\quad \times \left\{ \mathrm{dn}\left[ \pm\sqrt{\frac{\gamma^2}{A}} d_{\mathrm{core}} + X_0 \,\middle|\, m \right] \right\}. \end{aligned} \tag{19}$$

In equation (19), the sign in front of the square roots is related to the sign of $\epsilon_{zz}$ as we discussed before (see equation (16) and the text after). We remind the reader that $\epsilon_{xx}$ appears in equation (19) through $\mathrm{q}_{\mathrm{core}}^2$ that is used to define $Q$ (equation (13)) and consequently $\gamma^2$ and $\delta^2$ (equation (15)). Since we are searching for nonlinear bounded solutions with finite energy in the core, we will consider only the subcase with $q_{\mathrm{core}}^2 < 0$ and $C_0 > 0$ for negative $a_{\mathrm{nl}}^{\mathrm{EJEM}}$ (subcase which satisfies the condition shown in equation (11)) in the derivation of the nonlinear dispersion relation, and the other subcases (for $a_{\mathrm{nl}}^{\mathrm{EJEM}} < 0$) which provide unbounded solutions in the nonlinear core will be summarized in appendix A and table A1.

*3.1.2. Case $a_{\mathrm{nl}}^{\mathrm{EJEM}} > 0$:* Now we consider the case in which the effective parameters $\epsilon_{xx}$, $\epsilon_{zz}$, $\alpha_{xx}$, and $\alpha_{zz}$ provide positive values for the effective nonlinearity $a_{\mathrm{nl}}^{\mathrm{EJEM}}$ (see equation (6)). The situation shares common points with the isotropic configuration with focusing Kerr-type nonlinearity [15, 20], while the present anisotropic case is more general since it is not necessary to use focusing Kerr-type nonlinearity in order to get positive values of $a_{\mathrm{nl}}^{\mathrm{EJEM}}$, as can be inferred from equation (6). The isotropic case studied previously [20] can be seen as a special case of the current study. For $a_{\mathrm{nl}}^{\mathrm{EJEM}} > 0$, the nonlinear wave equation given by

equation (7) can be written as

$$\frac{\mathrm{d}H_y}{\sqrt{AC_0 + AQH_y^2 - H_y^4}} = \pm\sqrt{\frac{1}{A}}\,\mathrm{d}x \quad \text{for } q_{\mathrm{core}}^2 > 0, \tag{20a}$$

$$\frac{\mathrm{d}H_y}{\sqrt{AC_0 - AQH_y^2 - H_y^4}} = \pm\sqrt{\frac{1}{A}}\,\mathrm{d}x \quad \text{for } q_{\mathrm{core}}^2 < 0, \tag{20b}$$

with the parameters $A$ and $Q$ such that

$$A = \frac{2}{(k_0^2 a_{\mathrm{nl}}^{\mathrm{EJEM}})}, \text{ and } Q = \begin{cases} k_0^2 q_{\mathrm{core}}^2 & \text{for } q_{\mathrm{core}}^2 > 0, \\ k_0^2 |q_{\mathrm{core}}^2| & \text{for } q_{\mathrm{core}}^2 < 0. \end{cases} \tag{21}$$

This means that equations (20) take different forms according to the signs of the integration constant $C_0$ and the quantity $q_{\mathrm{core}}^2$.

For $\boldsymbol{q_{\mathrm{core}}^2 < 0}$: in this subcase, $C_0$ can only take positive values as can be inferred from equation (9) for $H_{\mathrm{left}} > 0$. In this subcase, the magnetic field profile $H_y$ will be written in terms of the bounded Jacobi elliptical function cn $[u|m]$ by integrating equation (20*b*) in the nonlinear core and using formula 17.4.52 from [33] such that

$$H_y(x) = \begin{cases} \delta\,\mathrm{cn}\left[+\sqrt{\frac{\gamma^2+\delta^2}{A}}\left(x + \frac{d_{\mathrm{core}}}{2}\right) + X_0 \,\middle|\, m\right] & \text{for } \epsilon_{zz} > 0, \\ \delta\,\mathrm{cn}\left[-\sqrt{\frac{\gamma^2+\delta^2}{A}}\left(x + \frac{d_{\mathrm{core}}}{2}\right) + X_0 \,\middle|\, m\right] & \text{for } \epsilon_{zz} < 0, \end{cases} \tag{22}$$

where

$$\gamma^2 = \frac{+AQ + \sqrt{(AQ)^2 + 4AC_0}}{2}, \quad \delta^2 = \frac{-AQ + \sqrt{(AQ)^2 + 4AC_0}}{2}, \quad m = \frac{\delta^2}{\gamma^2 + \delta^2} \text{ and } X_0 = \mathrm{cn}^{-1}\left[\frac{H_{\mathrm{left}}}{\delta} \,\middle|\, m\right]. \tag{23}$$

The choice of the sign in front of the square roots in equation (22) is related to the sign of $\epsilon_{zz}$ and it is treated as in the previous case $a_{\mathrm{nl}}^{\mathrm{EJEM}} < 0$ (see equation (18) and the text after, together with equation (20*b*)). In order to derive the nonlinear dispersion relation in this subcase, we use the magnetic field profile in the nonlinear core given by equation (22) and the field profile in the linear metal claddings (equation (8)), together with the continuity condition of the tangential components of the electromagnetic field at the right core/metal interface. The final expression of the nonlinear dispersion relation reads

$$\frac{-k_0\epsilon_{zz}q_m}{\epsilon_m}\,\mathrm{cn}\left[\mp\sqrt{\frac{\gamma^2+\delta^2}{A}}\,d_{\mathrm{core}} + X_0 \,\middle|\, m\right] \mp \sqrt{\frac{\gamma^2+\delta^2}{A}}\left\{\mathrm{sn}\left[\mp\sqrt{\frac{\gamma^2+\delta^2}{A}}\,d_{\mathrm{core}} + X_0 \,\middle|\, m\right]\right\} \times \left\{\mathrm{dn}\left[\mp\sqrt{\frac{\gamma^2+\delta^2}{A}}\,d_{\mathrm{core}} + X_0 \,\middle|\, m\right]\right\} = 0. \tag{24}$$

We choose the lower positive sign for $\epsilon_{zz} > 0$ and the upper negative sign for $\epsilon_{zz} < 0$ (see equation (22)).

For $\boldsymbol{q_{\mathrm{core}}^2 > 0}$: unlike the former subcase, the sign of the integration constant $C_0$ cannot be determined directly.

First, we consider $C_0 < 0$. The magnetic field profile in the nonlinear core can be obtained by integrating equation (20*a*) using formula 17.4.43 from [33] with the reduced parameters $A$ and $Q$ defined in equation (21) such that

$$H_y(x) = \begin{cases} \delta\,\mathrm{nd}\left[-\sqrt{\frac{\gamma^2}{A}}\left(x + \frac{d_{\mathrm{core}}}{2}\right) + X_0 \,\middle|\, m\right], & \text{for } \epsilon_{zz} > 0, \\ \delta\,\mathrm{nd}\left[+\sqrt{\frac{\gamma^2}{A}}\left(x + \frac{d_{\mathrm{core}}}{2}\right) + X_0 \,\middle|\, m\right], & \text{for } \epsilon_{zz} < 0, \end{cases} \tag{25}$$

where

$$\gamma^2 = \frac{AQ + \sqrt{(AQ)^2 - 4A|C_0|}}{2}, \quad \delta^2 = \frac{AQ - \sqrt{(AQ)^2 - 4A|C_0|}}{2}, \quad m = \frac{\gamma^2 - \delta^2}{\gamma^2}, \text{ and } X_0 = \mathrm{nd}^{-1}\left[\frac{H_{\mathrm{left}}}{\delta} \,\middle|\, m\right]. \tag{26}$$

It is worth mentioning that, according to the used parameters $A$, $Q$, and $C_0$ in this subcase, the arguments under the square roots in the definitions of $\gamma^2$ and $\delta^2$ shown in equation (26) are positive, which ensures that both $\gamma$ and $\delta$ are real quantities and the magnetic field profile provided by equation (25) is real. Using the magnetic field profile shown in equation (25) and proceeding as for the previous case $a_{\mathrm{nl}}^{\mathrm{EJEM}} < 0$, we can write the nonlinear dispersion relation as

$$\frac{-k_0\epsilon_{zz}q_m}{\epsilon_m}\,\mathrm{nd}\left[\mp\sqrt{\frac{\gamma^2}{A}}\,d_{\mathrm{core}} + X_0 \,\middle|\, \mathrm{m}\right] = \mp\sqrt{\frac{\gamma^2}{A}}\,(\mathrm{m})\left\{\mathrm{sd}\left[\mp\sqrt{\frac{\gamma^2}{A}}\,d_{\mathrm{core}} + X_0 \,\middle|\, \mathrm{m}\right]\right\} \times \left\{\mathrm{cd}\left[\mp\sqrt{\frac{\gamma^2}{A}}\,d_{\mathrm{core}} + X_0 \,\middle|\, \mathrm{m}\right]\right\}. \tag{27}$$

In equation (27), we choose the upper negative sign in front of the square roots for $\epsilon_{zz} > 0$, and we choose the bottom positive sign for $\epsilon_{zz} < 0$ (see equation (18) and the derivative of the Jacobi elliptical functions nd $[u, m]$ in [33]).

Second, for $C_0 > 0$, we can write the magnetic field profile in the nonlinear core as

$$H_y(x) = \begin{cases} \frac{\gamma\delta}{\sqrt{\gamma^2+\delta^2}}\mathrm{sd}\left[-\sqrt{\frac{\gamma^2+\delta^2}{A}}\left(x+\frac{d_{\mathrm{core}}}{2}\right)+X_0 \,\middle|\, m\right] & \text{for } \epsilon_{zz} > 0, \\ \frac{\gamma\delta}{\sqrt{\gamma^2+\delta^2}}\mathrm{sd}\left[+\sqrt{\frac{\gamma^2+\delta^2}{A}}\left(x+\frac{d_{\mathrm{core}}}{2}\right)+X_0 \,\middle|\, m\right] & \text{for } \epsilon_{zz} < 0, \end{cases} \tag{28}$$

where

$$\gamma^2 = \frac{-AQ+\sqrt{(AQ)^2+4AC_0}}{2},$$
$$\delta^2 = \frac{+AQ+\sqrt{(AQ)^2+4AC_0}}{2},$$
$$m = \frac{\delta^2}{\gamma^2+\delta^2}, \text{ and } X_0 = \mathrm{sd}^{-1}\left[\frac{H_{\mathrm{left}}\sqrt{\gamma^2+\delta^2}}{\gamma\delta}\,\middle|\, m\right]. \tag{29}$$

The associated nonlinear dispersion relation gives

$$\begin{aligned} &\frac{-k_0\epsilon_{zz}q_m}{\epsilon_m\sqrt{\gamma^2+\delta^2}}\left\{\mathrm{sn}\left[\mp\sqrt{\frac{\gamma^2+\delta^2}{A}}d_{\mathrm{core}}+X_0 \,\middle|\, m\right]\right\} \\ &\quad\times\left\{\mathrm{dn}\left[\mp\sqrt{\frac{\gamma^2+\delta^2}{A}}d_{\mathrm{core}}+X_0 \,\middle|\, m\right]\right\} \\ &\quad= \mp\sqrt{\frac{1}{A}}\,\mathrm{cn}\left[\mp\sqrt{\frac{\gamma^2+\delta^2}{A}}d_{\mathrm{core}}+X_0 \,\middle|\, m\right]. \end{aligned} \tag{30}$$

It is important to note that an alternative formula to equation (28) can also be obtained in terms of the Jacobi elliptical function cn $[u|m]$ as was already used in the isotropic case [20]. The choice of the sign of the nonlinear dispersion relation in equation (30) is linked to the sign of $\epsilon_{zz}$, as shown in equation (28), in which we choose the upper negative sign for $\epsilon_{zz} > 0$ and the lower positive one for $\epsilon_{zz} < 0$.

The nonlinear dispersion relations shown in equations (19), (24), (27), and (30) represent the full nonlinear dispersion relations for the bounded solutions propagating in the anisotropic nonlinear plasmonic slot waveguide depicted in figure 1 under the EJEM assumptions described in section 3.1. For fixed opto-geometrical parameters, the preceding nonlinear dispersion relations are solved for the real part of the effective index $\Re e(n_{\mathrm{eff}})$ to obtain the nonlinear dispersion diagrams.

### 3.2. Finite element method

In this part, we use the FEM-based model to solve the nonlinear TM eigenvalue problem in the one-dimensional anisotropic layered structure depicted in figure 1. It is well known that the FEM is generally versatile and can be applied to complex nonlinear waveguide problems, including two-dimensional ones with arbitrary shape and field profiles [44–47]. Generally speaking, in the frame of the FEM, the initial physical problem is transformed into a variational form (weak formulation) by multiplying the initial partial differential equation by chosen test functions that belong to a particular functional space. The next step is the discretization of the problem, in which the waveguide cross section is first divided into a patchwork of elements. The unknown fields are expanded in terms of interpolation polynomials over each element. The expansion coefficients that define the values of the fields at the nodal elements can then be obtained by solving a standard matrix eigenvalue problem. For a general and recent review of the finite element method in the frame of optical waveguides, the reader can refer to chapter 4 in [48].

In this article, in order to treat the anisotropic nonlinearity in the frame of our FEM, the fixed power algorithm [36, 44, 49] will be used, in which the input is the total power and the outputs are the field profile (the eigenfunction) and the corresponding effective index (the eigenvalue). This algorithm uses a simple iterative scheme based on a sequence of linear modal solutions which converge to the nonlinear solution after few steps. The fundamental issue is that the amplitudes of the eigenmode are irrelevant and the numerical solution of the intermediary eigenvalue problem used at each iteration has an uncontrolled amplitude. But, since the nonlinear problem depends on the amplitude of the field, the numerical eigenvector which is computed at each step as a solution of the eigenvalue problem has to be scaled by a scalar factor. This process allows the eigenvector to be used as input for the next iteration. The scaling factor is computed at each iteration for a fixed value of the input power. For the single-component eigenvalue problem written in terms of the magnetic field component $H_y$, an approximated formula has already been used [8, 21, 22, 36] in order to compute the scaling factor using only the linear part of the permittivity and neglecting the nonlinear term (see equation (B.2) in appendix B). Moreover, only the transverse component of the electric field was used in the isotropic Kerr-type nonlinearity. It is worth mentioning that it is not possible to take into account all the electric field components in the Kerr-type nonlinearity using the single-component eigenvalue problem [8] within the FEM implementation of the fixed power algorithm, as is demonstrated using equation (B.3) and the text after it.

In the current study, we present a new and generalized formalism for the fixed power algorithm in arbitrary nonlinear layered structures where the nonlinearity will be treated in a more rigorous way such that all the components of the electric field are taken into account in the Kerr-type nonlinearity and no assumptions are needed to compute the scaling factor. Additionally, unlike the previous isotropic cases [8, 21, 36, 44], we

consider a fully anisotropic nonlinear treatment for the permittivity tensor as it is shown in equation (1).

Our approach is based on the solution of a coupled nonlinear eigenvalue problem in terms of the continuous tangential components of the electromagnetic field $H_y$ and $E_z$. In order to obtain the correct weak formulation, we must consider the full TM wave equations with both the inhomogeneous permittivity term induced by the nonlinearity and the structure interfaces. The corresponding coupled weak formulation reads:

$$\begin{cases} \dfrac{-1}{k_0^2}\displaystyle\int_\Gamma \frac{1}{\epsilon_z(x)}\frac{\mathrm{d}h_y}{\mathrm{d}x}\frac{\mathrm{d}h_y'}{\mathrm{d}x}\mathrm{d}x + \int_\Gamma h_y(x)h_y'(x)\mathrm{d}x \\ - n_{\mathrm{eff}}^2\displaystyle\int_\Gamma \frac{1}{\epsilon_x(x)}h_y(x)h_y'(x)\mathrm{d}x = 0, \\ \displaystyle\int_\Gamma e_z(x)e_z'(x)\mathrm{d}x - \frac{1}{\epsilon_0 k_0 c}\int_\Gamma \frac{1}{\epsilon_z(x)}\frac{\mathrm{d}h_y}{\mathrm{d}x}e_z'\mathrm{d}x = 0. \end{cases} \tag{31}$$

Here, $h_y(x)$ and $e_z(x)$ stand for the tangential components of the magnetic and electric field, respectively, and $\Gamma$ is the domain of integration (in the present case the full cross section of the waveguide). In system (31) $\forall h_y'(x)$, $e_z'(x) \in \mathrm{H}_0^2(\Gamma)$ we look for $h_y(x)$, $e_z(x) \in \mathrm{H}_0^2(\Gamma)$, where $\mathrm{H}_0^2(\Gamma)$ is the Sobolev space of order 2 with null Dirichlet boundary conditions on the domain of integration $\Gamma$. It is important to point out that for the magnetic field $h_y$, we must pick a test function from a functional space (Sobolev space) at least of order 2, while, for the tangential component of the electric field $e_z$, we can choose a test function from a functional space of order 1 or 2 as can be understood from the relation between the tangential components shown in equation (2*b*). We use the fixed power algorithm described in algorithm 1 to solve the coupled eigenvalue problem shown in system (31). Our FEM is implemented using the free and open-source software `GMSH` as a mesh generator and `GETDP` as a solver [50–52]. These software programs have already been used to solve both one-dimensional and two-dimensional isotropic nonlinear electromagnetic waveguide problems [8, 21, 36]. It is worth mentioning that our FEM, with its fixed power algorithm shown in algorithm 1, can be reduced to take into account all EJEM assumptions as described in appendix B and as will be illustrated in the next section.

**Algorithm 1.** Fixed power algorithm to solve the coupled nonlinear eigenvalue problem depicted in equation (31).

1: We start with an initial guess $E_x^{\mathrm{init}}$, $E_z^{\mathrm{init}}$, which will be used to compute $\epsilon_x$ and $\epsilon_z$ from equation (1).

2: We use $\epsilon_x$ and $\epsilon_z$ in the coupled eigenvalue problem equation (31) to compute the eigenvectors $h_y$ and $e_z$ with the corresponding eigenvalue $n_{\mathrm{eff}}$. The outputs will be used to compute the rescaling factor $\chi$ for a given fixed value of the power $P_{\mathrm{tot}}$ which can be derived from the longitudinal $z$ component of the pointing vector integrated over the transverse $x$-direction and using equation (2*c*) such that

$$P_{\mathrm{tot}} = \frac{\chi^2}{2k_0\Re e(n_{\mathrm{eff}})}\int_\Gamma \left[\frac{\mathrm{d}e_z(x)}{\mathrm{d}x} + \omega\mu_0 h_y(x)\right]h_y(x)\mathrm{d}x.$$

(Continued.)

3: The rescaling factor $\chi$ will be used to compute the correct amplitude of the longitudinal components such that $H_y = \chi h_y$ and $E_z = \chi e_z$. The transverse component of the electric field $E_x$ will be computed from equation (2*c*) using $H_y$ and $E_z$. The updated effective nonlinear permittivities $\epsilon_x$ and $\epsilon_z$ will be used as inputs for the next iteration.

4: We repeat steps (2) and (3) until the following criterion is satisfied: $|\Re e(n_{\mathrm{eff}}^i) - \Re e(n_{\mathrm{eff}}^{i-1})|/|\Re e(n_{\mathrm{eff}}^i)| < \delta \quad \forall i \in [1, N]$, where $\Re e(n_{\mathrm{eff}}^i)$ is the eigenvalue for the step $i$ and N is the step number in the procedure. We set $\delta = 10^{-5}$ such that, in order to fulfill the criterion, between 10 and 15 steps are needed depending on the waveguide parameters and the initial field used.

## 4. Numerical results

In this section, we present several numerical results to validate our models and to demonstrate the influence of the anisotropy on the nonlinear dispersion diagrams and on the effective nonlinearity. We build nonlinear cores from stacks of realistic bulk materials, and we use the effective medium theory (EMT) to retrieve their linear and nonlinear effective parameters [23, 53]. Moreover, we assume that both $d_1$ and $d_2$ (see figure 1(b)) are much smaller than the operating wavelength, so we can derive the effective linear permittivities and the effective nonlinear susceptibilities in the frame of the simple EMT [23, 53]:

$$\begin{aligned} \tilde{\epsilon}_{zz} &= r\epsilon_2 + (1-r)\epsilon_1, \\ \tilde{\epsilon}_{xx} &= \frac{\epsilon_1\epsilon_2}{r\epsilon_1 + (1-r)\epsilon_2}, \\ \tilde{\alpha}_{zz} &= 3(r\chi_2^{(3)} + (1-r)\chi_1^{(3)}), \\ \tilde{\alpha}_{xx} &= 3\frac{r\chi_2^{(3)}\epsilon_1^2 + (1-r)\chi_1^{(3)}\epsilon_2^2}{((1-r)\epsilon_2 + r\epsilon_1)^2}. \end{aligned} \tag{32}$$

where $r = d_2/(d_1 + d_2)$ is the ratio of the second material in the core, $\epsilon_j$ and $\chi_j^{(3)}$, $j \in \{1, 2\}$ are the linear permittivities and third-order nonlinear susceptibilities of the constituent materials used in the core, respectively. Generally, $\tilde{\epsilon}_{jj} = \epsilon_{jj} + \mathrm{i}\epsilon_{jj}''$ and $\tilde{\alpha}_{jj} = \alpha_{jj} + \mathrm{i}\alpha_{jj}''$ are complex; the real parts are used in the derivation of the models whereas the imaginary parts will be used to estimate the losses. In this study, we will consider only the linear losses; nonlinear processes like two-photon absorption are neglected [54, 55]. The imaginary part of the effective indices $\Im m(n_{\mathrm{eff}})$ will be estimated using the method based on the field profiles and imaginary parts of the permittivity described in [8, 35, 37] for the isotropic case. It is worth noting that this method has already been used to estimate the losses in isotropic nonlinear plasmonic waveguides [8, 21, 37]. In formula (33), we provide the extension of this method to the anisotropic case:

$$\begin{aligned} \Im m(n_{\mathrm{eff}}) = &\frac{\epsilon_0 c}{4P_{\mathrm{tot}}}\left[\int_{\mathrm{core}} \epsilon_{xx}''|E_x(x)|^2 + \epsilon_{zz}''|E_z(x)|^2\mathrm{d}x\right] \\ &+ \frac{\epsilon_0 c}{4P_{\mathrm{tot}}}\left[\int_{\mathrm{cladding}} \epsilon_m''(|E_x(x)|^2 + |E_z(x)|^2)\mathrm{d}x\right]. \end{aligned} \tag{33}$$

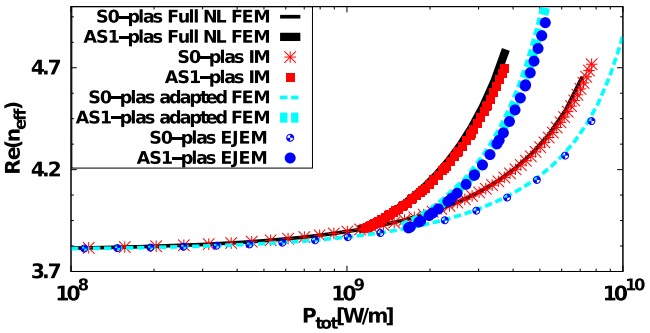


**Figure 2.** Comparison between the nonlinear dispersion curves for the NPSW depicted in figure 1 reduced to the fully isotropic case by setting $r = 0$ in equation (32), with $\epsilon_1 = 3.46^2 + i10^{-4}$ and $\alpha_{zz} = \alpha_{xx} = 6.36 \times 10^{-19}$ m$^2$ V$^{-2}$ [15].

Here, $P_{\text{tot}}$ is the total power and $\epsilon_m''$ is the imaginary part of the metal cladding permittivity. For the numerical results presented below, the core thickness is fixed at $d_{\text{core}} = 400$ nm, and we use gold for the metal claddings with $\tilde{\epsilon}_m = -90 + \text{i}10$ at $\lambda = 1.55$ $\mu$m [56]. First, we simplify our models to the isotropic case and compare the results with previously published works. For the anisotropic case, we use the classification shown in section 3.1 for $a_{\text{nl}}^{\text{EJEM}} < 0$ and $a_{\text{nl}}^{\text{EJEM}} > 0$ depending on the values and the signs of the linear and the nonlinear permittivity terms (see equation (6)). It is worth noting that this classification is more general than the one shown in our recent work [29], where $\alpha_{xx} = \alpha_{zz} = \alpha > 0$ and $\epsilon_{xx} \neq \epsilon_{zz}$, in which we classified the problem according to the signs of the linear permittivity tensor terms into elliptical and hyperbolic cases only. This previous splitting can be seen as a special case of the current more general classification. In section 4.4, we show that the classification of the nonlinear solutions according to the sign of $a_{\text{nl}}^{\text{EJEM}}$ given by equation (6) and derived in the frame of the EJEM cannot be extended to all the possible solutions computed within the full NL FEM due to the assumptions of the EJEM.

### *4.1. Isotropic case: validation and comparison with [15, 20]*

We begin with the isotropic case, considering a nonlinear isotropic core with a focusing Kerr-type nonlinearity, and we compare the results with [15, 20] using exactly the same parameters. In this case, we set $r = 0$ in equation (32), and the isotropic nonlinear material in the core corresponds to amorphous hydrogenated silicon with $\epsilon_1 = 3.46^2 + \text{i}10^{-4}$ with the nonlinear parameter being $\alpha_{zz} = \alpha_{xx} = 6.36 \times 10^{-19}$ m$^2$ V$^{-2}$, which is related to the nonlinear refractive index $n_2$ through $n_2 \approx \alpha_{xx}/(\epsilon_0 c \Re e(\epsilon_1))$ [15, 20]. In figure 2, we study the nonlinear dispersion curves for the fundamental nonlinear symmetric mode denoted by S0-plas (thin lines, small circles, and cross points) and the first nonlinear asymmetric mode AS1-mode (thick lines, big closed circles, and squares), which bifurcates from the S0-plas mode at the critical power value. The asymmetric mode AS1-mode has no counterpart in the linear case and it exists only above a certain threshold as a signature of a strong spatial nonlinear effect [15, 19, 57]. This kind of bifurcation is called Hopf bifurcation and it has already been observed in the simple nonlinear plasmonic slot waveguide [11, 15, 20] and in its improved version [21, 22]. We begin with comparing the results obtained from the FEM described in section 3.2 and denoted full NL FEM in the following, taking into account all the contributions of the electric field in the Kerr nonlinearity (black curves) with the results obtained from the interface model (IM) (represented by the red curves in figure 2) [20]. The IM is a numerical method developed specifically for the nonlinear isotropic slot waveguides [15, 20], where all the non-null electric field components are present in the Kerr nonlinearity. One clearly sees that the results obtained from our full NL FEM, with its coupled formulation (see section 3.2), agree well with the results acquired using the IM. Next, we compare the results obtained from the EJEM-adapted FEM presented in appendix B taking into account all the assumptions of the EJEM (dashed cyan curves), with the results obtained from the semi-analytical approach EJEM described in section 3.1 (blue circles). Once again, one clearly sees that the results from our adapted FEM recover the results from the semi-analytical EJEM. In figure 2, at high powers, there exist some discrepancies between the results obtained from the methods which consider the full treatment of the nonlinearity (FEM full NL (black) and IM (red) curves) in the core and the results obtained in the frame of the EJEM approximations (adapted FEM (cyan) and EJEM (blue) curves). These discrepancies are due to the simplified way used to describe the nonlinearity in the EJEM models (see section 3.1). However, the results which are based on the EJEM assumptions can predict the behaviour of the nonlinear dispersion curves as can be inferred from figure 2.

Another important remark is that our two FEMs are based on the fixed power algorithm in which, for a given input power, we look for the corresponding effective index of the investigated nonlinear mode (see section 3.2). This means that they fail to follow the branches of the nonlinear dispersion curves with a negative slope, which usually correspond to unstable modes (see figure 1 in [15]). The current versions of the FEM based on the fixed power algorithm converge only to possibly stable modes [45, 58].

### *4.2. Anisotropic case with $a_{\text{nl}}^{\text{EJEM}} < 0$: results and validation*

In this subsection, we present one example for the case in which the effective nonlinearity $a_{\text{nl}}^{\text{EJEM}}$ is negative (see section 3.1.1), and we compare the results obtained from the semi-analytical approach EJEM with those acquired from the full NL FEM and from the adapted FEM to match the EJEM assumptions (see appendix B). As we have mentioned before, the sign of $a_{\text{nl}}^{\text{EJEM}}$ (see equation (6)) depends on the linear and nonlinear effective parameters of the core. In this example, we choose the two materials in the core in order to get a negative effective nonlinearity. We use silver for material 2 with $\epsilon_2 = -129 + \text{i}3.28$ [59]. Due to the imaginary part of $\epsilon_2$, it is important to use a gain medium for material 1 (with permittivity $\epsilon_1$) in order to compensate for the metal losses. Chalcogenide glass is a promising candidate since it can act as a gain medium at the telecommunication wavelength; in addition, it has a high nonlinear coefficient and a low two-photon

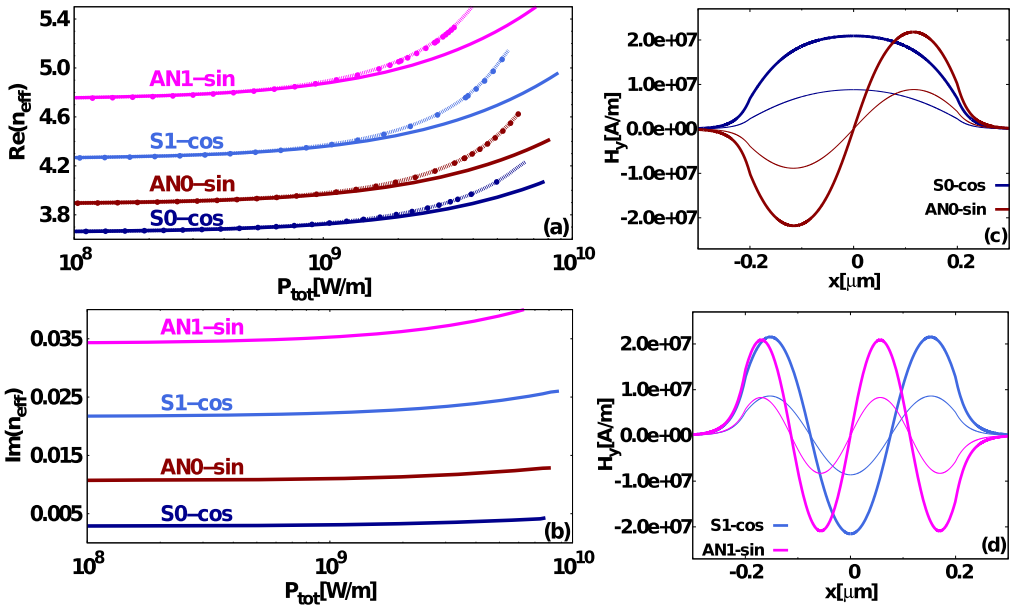


**Figure 3.** (a) Nonlinear dispersion curves in the anisotropic case for $a_{\mathrm{nl}}^{\mathrm{EJEM}} < 0$ (see the text for the parameters used). Solid lines show the full NL FEM, broken lines show the adapted FEM, and closed circles show the semi-analytical EJEM. (b) $\Im m\,(n_{\mathrm{eff}})$ as a function of $P_{\mathrm{tot}}$ for the results obtained with full NL FEM. (c) $H_y$ component for the symmetric S0-cos main mode and the antisymmetric AN0-sin main mode at two different power values; thin curves show $P_{\mathrm{tot}} = 10^9$ W m$^{-1}$ and thick curves show $P_{\mathrm{tot}} = 6 \times 10^9$ W m$^{-1}$. (d) Similar to (c) but for higher-order modes: symmetric S1-cos and antisymmetric AN1-sin.

absorption at this wavelength, compared to the usual semiconductors [60, 61]. Thus, the permittivity of material 1 is set at $\epsilon_1 = 2.47^2 - \mathrm{i}0.0072$, corresponding to very small gain. The third-order nonlinear susceptibility of material 1 is set at $\chi_1^{(3)} \approx 1.08 \times 10^{-19}$ m$^2$ V$^{-2}$ [54]. We will omit the nonlinearity of material 2 (silver) since it is weak compared to that of the chalcogenide glass at $\lambda = 1.55$ $\mu$m. It is worth mentioning that the idea of loss compensation in metal/dielectric multilayer structures has already been investigated theoretically [62, 63] and demonstrated experimentally [64, 65]. In order to compute the effective parameters in the core, we set $r = 0.5$ in equation (32), which gives us $\tilde{\epsilon}_{xx} = 12.80 + \mathrm{i}0.00029$, $\tilde{\epsilon}_{zz} = -61.449 + \mathrm{i}1.63633$, $\alpha_{xx} = 7.13 \times 10^{-19}$ m$^2$ V$^{-2}$, and $\alpha_{zz} = 1.62 \times 10^{-19}$ m$^2$ V$^{-2}$. One clearly sees that the imaginary part of the longitudinal linear component, $\epsilon''_{zz}$, is not null. This observation is fully coherent with the results provided in [66] that deal with semiconductor as gain medium in linear waveguides with hyperbolic dispersion properties. In figure 3(a), we present the nonlinear dispersion diagram for $\Re e\,(n_{\mathrm{eff}})$ as a function of the total power for $a_{\mathrm{nl}}^{\mathrm{EJEM}} < 0$ using the semi-analytical EJEM described in section 3.1.1 (closed circles) and full NL FEM with the full treatment of the Kerr nonlinearity (solid lines), and the adapted FEM shown in appendix B (broken lines). At low powers, when the assumptions of the EJEM are valid, the dispersion curves acquired by the three methods are identical. Nevertheless, as expected, at high powers, when the EJEM assumptions are not fully valid, we obtain some discrepancies between the full NL FEM (solid lines) and the methods based on the EJEM assumptions (broken lines for adapted FEM and closed circles for EJEM). It is worth noticing that the adapted FEM actually reproduces the results obtained from the semi-analytical EJEM, even at high powers; this can be seen as a validation of our methods. Due to the negative effective nonlinearity, we observe a defocusing behaviour inside the nonlinear core, starting from a positive third-order nonlinear susceptibility of material 1; figures 3(c) (main symmetric and antisymmetric modes) and 3(d) (first symmetric and antisymmetric higher-order modes) illustrate this phenomenon. In figure 3(b), we estimate the losses using the results obtained from the more accurate model full NL FEM. The $\Im m\,(n_{\mathrm{eff}})$ is computed using equation (33), and we observe an increase of $\Im m\,(n_{\mathrm{eff}})$ with the increase of power for the modes under investigation. This is due to the defocusing behaviour in the core, where the field profiles tend to be more located in the metal claddings with the increase of power (see figures 3(c) and (d)). It is worth mentioning that in this case we did not observe a bounded asymmetric mode due to the defocusing effect in the core (see the end of section 3.1.1 and appendix A). To conclude on this point, we have presented one example for the case in which the effective nonlinearity is negative and have validated the methods developed in this study. Moreover we have found that, in this example, starting from a positive Kerr-type nonlinearity, we observe a defocusing behaviour in the core. Different parameters can be chosen in equation (6) in order to obtain a negative effective nonlinearity; this nevertheless does not affect the validation of our models.

### *4.3. Anisotropic case with $a_{\mathrm{nl}}^{\mathrm{EJEM}} > 0$: results and validation*

In this subsection, we present a numerical example for the anisotropic case in which $a_{\mathrm{nl}}^{\mathrm{EJEM}} > 0$. We choose material 1 with $\epsilon_1 = 3.46^2 + \mathrm{i}10^{-4}$ and $\chi_1^{(3)} \approx 2.122 \times 10^{-19}$ m$^2$ V$^{-2}$ (amorphous hydrogenated silicon [15, 20]). For the second material in the core with permittivity $\epsilon_2$, we consider an ideal ENZ material with $\Re e\,(\epsilon_2) \approx 0$ and $\Im m\,(\epsilon_2) \approx 0$. This choice

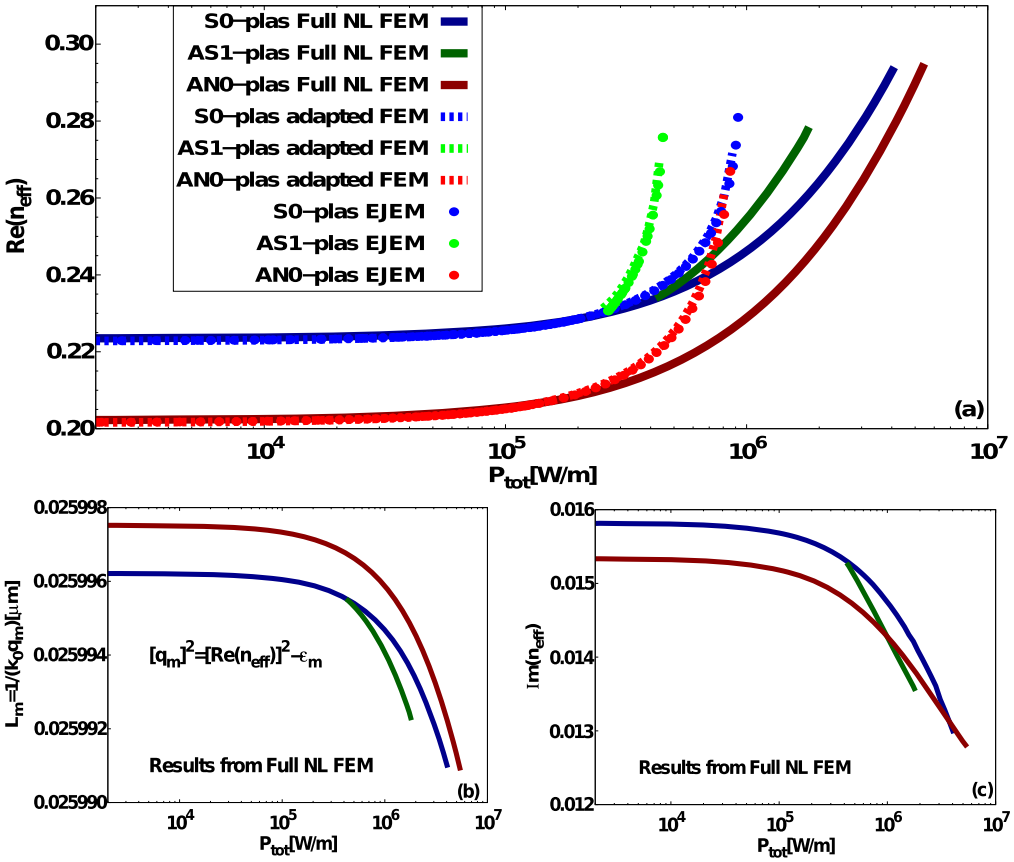


**Figure 4.** (a): Nonlinear dispersion curves for $a_{\mathrm{nl}}^{\mathrm{EJEM}} > 0$ using EJEM (closed circles), the adapted FEM (broken lines), and full NL FEM (dark solid lines). Blue, green, and red lines represent symmetric, asymmetric, and antisymmetric modes, respectively. (b): Attenuation length in the metal claddings computed using the results obtained from full NL FEM, with $\epsilon_m = -90$ being the real part of the metal cladding permittivity. (c): $\Im m\,(n_{\mathrm{eff}})$ using the results obtained from full NL FEM; the corresponding $\Re e\,(n_{\mathrm{eff}})$ are shown in (a). In this figure, the effective nonlinear susceptibility parameters $\alpha_{xx}$ and $\alpha_{zz}$ are not equal (see text for the parameters used).

of the second material is justified, since it was recently shown [67] that for the usual ENZ materials with $\Re e\,(\epsilon_2) \approx 0$ and $\Im m\,(\epsilon_2) > \Re e\,(\epsilon_2)$, the fundamental principle of causality leads to diverging energy-loss function and that the loss cannot be compensated even with huge gain values. A typical example for such usual ENZ materials with null real part and small imaginary part of the permittivity is indium-tin oxide [28]. Furthermore, it is demonstrated theoretically [67] that in order to make use of the properties of the ENZ materials in waveguide problems, they must have a vanishing imaginary part of the permittivity (ideal ENZ). In our study, the ideal ENZ permittivity (material 2 in the core) will be obtained by considering a mixture of aluminium-doped zinc oxide (AZO)-coated quantum dots dispersed in a polymer matrix; the resulting permittivity is retrieved using Maxwell–Garnett's relation. This technique is similar to what has been used in [68], while here we use spherical AZO-coated quantum dots instead of the spherical Ag-coated quantum dots. The spherical AZO-coated quantum dots in our study consist of AlGaAsP (gain medium with permittivity 11.8−i0.16) as an inner core medium and AZO as an outer shell with permittivity −8+i0.1. Using Maxwell–Garnett's formula [68] with a filling ratio set to 0.08, we obtain the permittivity of the spherical AZO-coated quantum dots $\epsilon_{\mathrm{QDs}} = -1.42 + \mathrm{i}0.0006$. The next step in obtaining the permittivity of material 2 is to insert the spherical AZO-coated quantum dots within a polymer matrix (PMMA) with $\epsilon_{\mathrm{PMMA}} = 2.66$ with a filling ratio equal to 0.475 such that using Maxwell–Garnett's relation, the permittivity of material 2 reads $\epsilon_2 = 0.0043 + \mathrm{i}0.000555$ with the third-order nonlinear coefficient of the second material being $\chi_2^{(3)} \approx 3.0 \times 10^{-20}$ $\mathrm{m}^2\,\mathrm{V}^{-2}$, similar to the one used in [39]. It is worth mentioning that a similar procedure has already been used to obtain an ideal ENZ material using quantum dots [39] for a metamaterial multilayer structure with an isotropic dielectric response, unlike the current study. The permittivity of material 2 will be used together with that of material 1 to obtain the effective parameters in the core using equation (32). We choose $r = 0.1$ to obtain $\tilde{\epsilon}_{xx} = 0.043 + \mathrm{i}0.005$, $\tilde{\epsilon}_{zz} = 10.77 + \mathrm{i}0.00014$, $\alpha_{xx} = 8.94 \times 10^{-19}\,m^2/V^2$, and $\alpha_{zz} = 5.82 \times 10^{-19}\,m^2/V^2$. In figure 4(a), we present the nonlinear dispersion curves for the three main modes: symmetric (blue), asymmetric (green), and antisymmetric (red) obtained using the EJEM (closed circles), the adapted FEM to match the EJEM assumptions (broken lines) and with full NL FEM taking into account the full treatment of the nonlinearity (dark solid curves). One can observe that the three methods coincide at low powers whereas, at high power, there exist some discrepancies between them. Once again, this can be understood from the assumptions of the EJEM. In

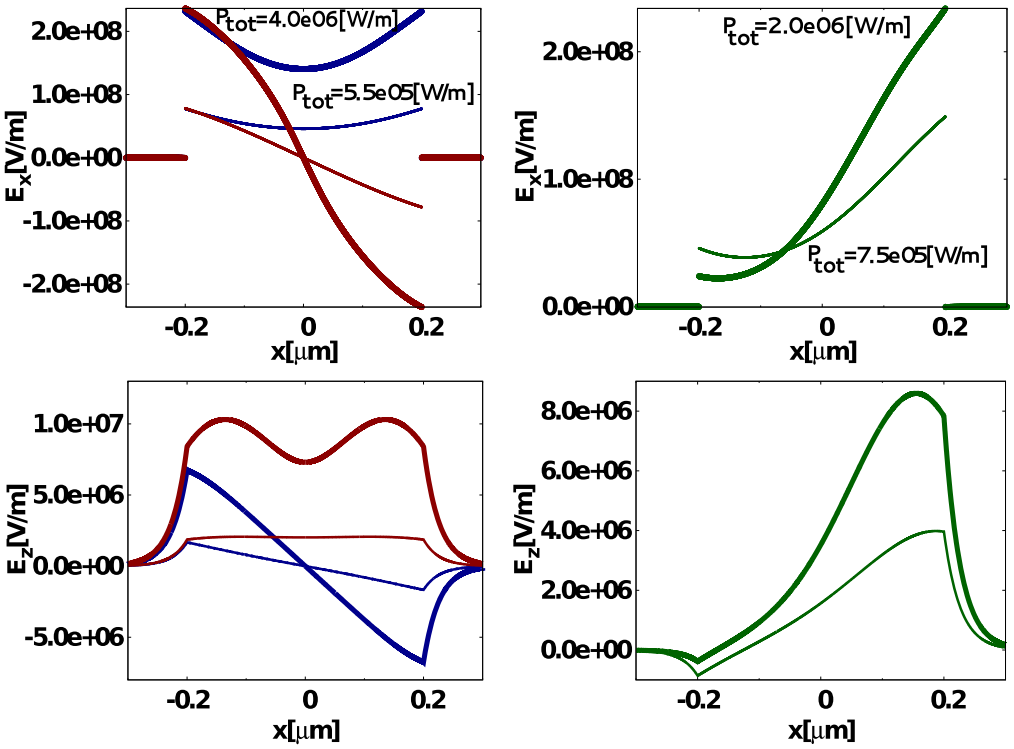


**Figure 5.** $E_x$ (first raw) and $E_z$ (second raw) components for the main modes computed using the more accurate model full NL FEM represented by the solid curves shown in figure 4(a). First column: nonlinear symmetric (dark blue), and antisymmetric (dark red) modes at two different power values (thin curves at $P_{\text{tot}} = 5.5e05$ W m$^{-1}$, solid curves at $P_{\text{tot}} = 4.0e06$ W m$^{-1}$). Second column: nonlinear asymmetric mode located at the right interface at two different power values (thin curves at $P_{\text{tot}} = 7.5e05$ W m$^{-1}$, solid curves at $P_{\text{tot}} = 2.0e06$ W m$^{-1}$).

addition, the EJEM (closed circles) and the adapted FEM (broken lines) are identical even at high powers, which confirms that the discrepancies between the methods at high powers are due to the assumptions of the EJEM. All the methods predict a huge reduction of the bifurcation threshold compared to the isotropic case shown in figure 2; typically in this anisotropic case, the bifurcation threshold is reduced by more than three orders of magnitude (see green curves in figure 4(a)), which is a signature of strong reinforcement of the spatial nonlinearity. This enhancement of the spatial nonlinearity can be understood qualitatively in equation (6) for an ENZ $\epsilon_{xx}$ and $\epsilon_{zz} \gg 1$. For a more detailed study of the influence of the linear anisotropic part of the permittivity tensor with an isotropic nonlinear term, unlike the current study, we refer to [29]. Other interesting consequences of using an ENZ $\epsilon_{xx}$ and $\epsilon_{zz} \gg 1$ are the very small effective indices obtained for the modes under investigation (see figure 4(a)), which have a direct influence on the field profiles in the metal claddings. This influence can be seen from the attenuation parameter in the metal which is quantified by $q_m^2 = ([\Re e\,(n_{\text{eff}})]^2 - \epsilon_m)$, where $\epsilon_m = -90$ is the real part of the metal cladding permittivity. In this case, $|\epsilon_m| \gg [\Re e\,(n_{\text{eff}})]^2$ even with the increase of $\Re e\,(n_{\text{eff}})$ at high powers, and $q_m^2$ remains nearly constant. This means that the increase in power has a negligible effect on the field profiles in the linear metal claddings, and the attenuation length in the metal $L_m = 1/(k_0 q_m)$ remains nearly constant with the increase in power as can be seen in figure 4(b) ($L_m$ is constant up to five digits). In this figure, the attenuation length slightly decreases ($q_m$ slightly increases) for all the modes under investigation. Consequently, with the increase in power, the field profiles will be more localized at the core metal interfaces with a nearly constant portion in the metal claddings (see figure 5). Therefore, the overall losses slightly decrease with the increase in power, as can be seen in figure 4(c). It is worth mentioning that this interesting property cannot be obtained in the usual isotropic NPSWs, where the losses increase with the power [15]. In figure 5, we present the $E_x$ and $E_z$ components for the symmetric (blue), asymmetric (green), and antisymmetric (red) modes obtained from full NL FEM. On the one hand, the field profiles in the metal claddings are nearly constant as we discussed previously; on the other hand, the intensities at the metal/core interfaces increase with power. Consequently, the losses decrease with the increase in power, as is shown in figure 4(c). We focused only on the main modes; higher-order modes exist and they are quite similar to those obtained in the isotropic case [15]; however, due to the enhancement of the nonlinearity, these nonlinear higher-order modes appear at lower powers compared to the isotropic case. Their full investigation is beyond the scope of this study.

### 4.4. Beyond the EJEM assumptions

We have seen in sections 4.1–4.3 that the results obtained from the semi-analytical EJEM and the adapted FEM qualitatively agree with the results obtained from the more accurate model full NL FEM. More precisely, when the EJEM assumptions shown in section 3.1 are valid, the three methods produce the same results. Nevertheless, when the EJEM assumptions start

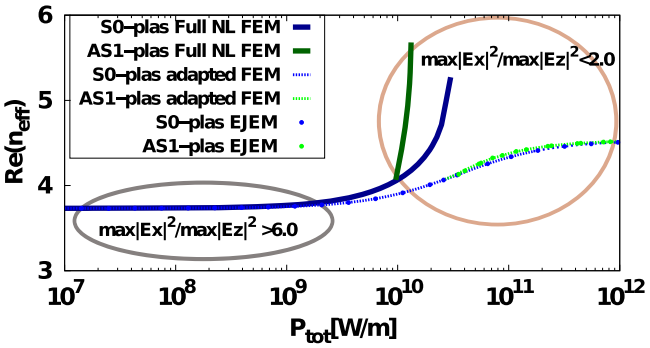


**Figure 6.** Nonlinear dispersion curves for the anisotropic case with $\epsilon_{xx} = 3.46^2$, $\epsilon_{zz} = 5.0$, and $\alpha_{xx} = \alpha_{zz} = 3.18 \times 10^{-19}$ m$^2$ V$^{-2}$. Solid lines show the results obtained from the full NL FEM, closed circles show results from EJEM, and broken lines show results from the adapted FEM. Blue and green represent nonlinear symmetric S0-plas and nonlinear asymmetric AS1-plas, respectively.

to be partially not valid (at high powers), we have found some discrepancies between the results obtained from the three methods (see figures 2–4). However, the global behaviour of the nonlinear dispersion curves remains the same. Consequently, using the semi-analytical EJEM, we were able to get more insights into the computed nonlinear solutions. In this subsection, we present a numerical example for the anisotropic case in order to show the limitations of the semi-analytical EJEM. In figure 6, we choose $\epsilon_{xx} = 3.46^2$, $\epsilon_{zz} = 5.0$, and $\alpha_{xx} = \alpha_{zz} = 3.18 \times 10^{-19}$ $m^2/V^2$. In this case, the effective nonlinearity in the EJEM framework is positive $a_{\mathrm{nl}}^{\mathrm{EJEM}} > 0$. We consider only the nonlinear symmetric (S0-plas) and asymmetric (AS1-plas) modes in this discussion. At low powers, when the transverse component of the electric field $E_x$ is much higher than the longitudinal one $E_z$, all the methods coincide. However, at high powers, we clearly see that the results obtained from the full NL FEM (solid curves) differ quantitatively from the results obtained from the EJEM (closed circles) and from the adapted FEM (broken lines) since at high powers, unlike figures 2–4, the ratio $\max |E_x|^2/|E_z|^2$ is less than 2.0. This inequality means that the amplitude of $E_z$ is comparable to the one of $E_x$, implying that the main assumption of the EJEM (that the Kerr nonlinearity depends only on $E_x$) is no longer valid. In the full NL FEM, we take into account both $E_x$ and $E_z$ in the Kerr-type nonlinearity. This example indicates that the classification of the nonlinear solutions according to the sign of $a_{\mathrm{nl}}^{\mathrm{EJEM}}$ given by equation (6) and derived in the frame of the EJEM cannot be extended to all the possible solutions computed within the full NL FEM. Nevertheless, this classification remains useful since it covers a wide range of configurations and, being analytical, it is straightforward to define it. This remark illustrates the complementarity of the two methods we described and validated in this study.

### *4.5. Numerical simulations of the nonlinear propagation in the time domain*

In our previous works [15, 21], we were able to use the nonlinear capabilities of the FDTD method implemented in the MEEP software [69, 70] to investigate the nonlinear propagation in isotropic NPSWs with or without buffer layers between the nonlinear and metal claddings. In the present study, the needed simulations are more difficult to realize due to the anisotropy (see, for example, [71]); nevertheless, some nonlinear anisotropic configurations can be modelled using the FDTD method as will be shown. The metal permittivity of the cladding is described by a Drude model to obtain the fixed negative value used at the studied wavelength. The useful computational domain is surrounded at its four edges by absorber regions that prevent back-reflected fields more efficiently than the perfectly matched layers that have also been tested during our FDTD simulations. In order to have reference results, we do not use the structure parameters given in the previous section but rather those provided in [15], where we have provided a detailed FDTD study for an isotropic NPSW with a positive Kerr-type nonlinearity. In our new simulations, the anisotropy is introduced by decreasing the $\varepsilon_{xx}$ values and keeping identical all the other parameters. This configuration corresponds to the generic case $a_{\mathrm{nl}}^{\mathrm{EJEM}} > 0$ that is studied in section 4.3.

First, we validate the anisotropic case for the FDTD simulations by computing the effective index in the linear case (nullifying the nonlinear coefficient) and comparing it with the results provided by our full NL FEM. For the first test case denoted in the following by (1), we obtain $\Re e\,(n_{\mathrm{eff}}^{\mathrm{FDTD}}) = 1.4772$ and $\Re e\,(n_{\mathrm{eff}}^{\mathrm{FEM}}) = 1.4996$. For the second case denoted by (2), which represents a strongly anisotropic configuration, we got $\Re e\,(n_{\mathrm{eff}}^{\mathrm{FDTD}}) = 1.034$ versus $\Re e\,(n_{\mathrm{eff}}^{\mathrm{FEM}}) = 1.040$. The parameters for these two cases are given in the legend of figure 8. In the isotropic, we have already noticed that the agreement between the two methods can be good if the resolution is high enough in the FDTD simulations. The comparison between the $H_y$ profiles obtained from the full NL FEM and the FDTD method for case (2) is shown in figure 7. In these anisotropic cases, we observed the convergence of the linear FDTD field profiles with higher resolutions toward those computed from the FEM as we did already in the isotropic case [15]. We fixed the resolution in the nonlinear FDTD simulations to the one used to get the previous results (180 grid cells per micrometre). As can be seen in figure 7(b), the agreement between the FDTD and the FEM results obtained for the strongly anisotropic case (2) are also good in the nonlinear case even if, at even higher powers, the discrepancies increase as has already been observed in the isotropic case.

In figure 8, we show the nonlinear propagation of the main symmetric mode S0-plas in the anisotropic NPSWs shown in figure 1, obtained using the FDTD method implemented in the MEEP software, for the two cases of anisotropy (1) and (2) defined in the previous paragraph. The sinusoidal phase modifications are clearly visible in these two plots. These results numerically demonstrate the stability up to the intermediate power regime of the main symmetric mode in the anisotropic NPSW with $\varepsilon_{zz} > \varepsilon_{xx} > 0$ and $a_{\mathrm{nl}}^{\mathrm{EJEM}} > 0$ (positive effective Kerr-type nonlinearity). This result is important for the possible applications since it is in this power regime where they can be designed and used. At higher powers, either the solutions are not numerically stable or the mode itself is not stable, as we have already observed in the isotropic case. We

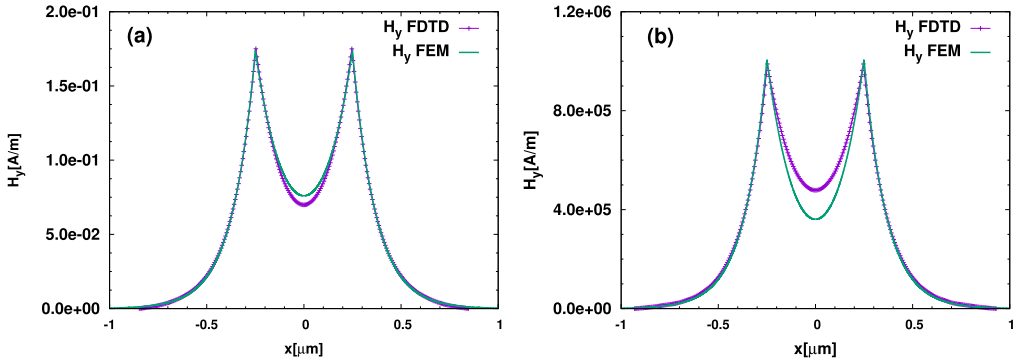


**Figure 7.** Field profiles of the $H_y$ component computed from the FDTD and from the full NL FEM for the strongly anisotropic test case (2). (a): Linear case, $\Re e\,(n_{\text{eff}}^{\text{FDTD}}) = 1.034$ and $\Re e\,(n_{\text{eff}}^{\text{FEM}}) = 1.040$. (b): Nonlinear case for a total power near $51 \cdot 10^6$ W m$^{-1}$, $\Re e\,(n_{\text{eff}}^{\text{FDTD}}) = 1.1857$, and $\Re e\,(n_{\text{eff}}^{\text{FEM}}) = 1.1850$.

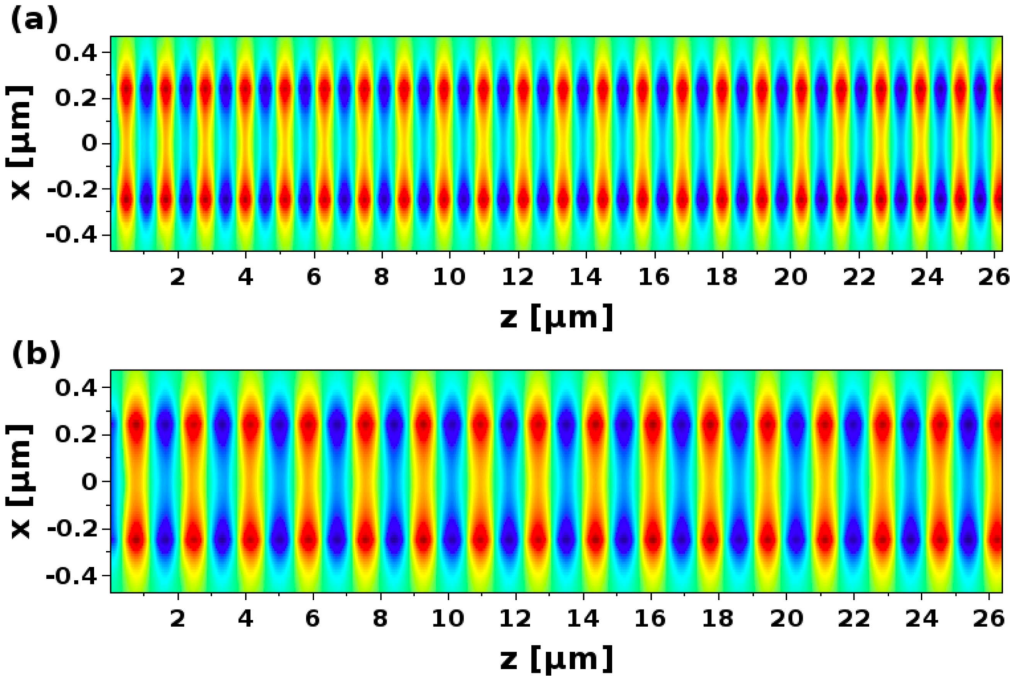


**Figure 8.** Evolution of the $H_y$ field profile for the symmetric S0-plas mode for the (1) weak anisotropic and (2) strong anisotropic cases. The simulations were realized using the FDTD method implemented in the MEEP software. The common parameters are as follows: core thickness $d = 500$ nm, metal permittivities $\epsilon_1 = \epsilon_3 = -6$ at a free-space wavelength $\lambda = 2.0$ $\mu$m, second-order nonlinear refractive index $n_{2,1}^{(2)} = 2 \cdot 10^{-17}$ m$^2$/W, $\epsilon_{yy} = \epsilon_{zz} = 3.80318$. (a): Case (1), in which $\epsilon_{xx} = 1.10307$ and the extracted effective index is $\Re e\,(n_{\text{eff}}) = 1.7128$). (b) Case (2), in which $\epsilon_{xx} = 0.56318$ and the extracted effective index is $\Re e\,(n_{\text{eff}}) = 1.1858$.

also notice that the effective indices computed with the FDTD do not correspond exactly to those computed using the full NL FEM, and the higher the power, the larger the difference. This remark was already made in our previous FDTD study dedicated to isotropic NPSWs. A more detailed FDTD investigation of the other main modes, including the first asymmetric and anti-symmetric modes, would be of interest but is beyond the scope of the present work, as NPSW configurations with an even higher anisotropy can be a serious issue from the numerical analysis point of view [71].

## 5. Conclusion

We have presented two different models for studying the stationary TM nonlinear solutions propagating in slot plasmonic waveguides with a nonlinear anisotropic metamaterial core. The first is a semi-analytical model in which we describe the nonlinear electromagnetic field components in the waveguide by the Jacobi elliptical functions; it extends to the anisotropic case our previous model valid only for isotropic configurations. Within this model, we have studied the nonlinear dispersion relations for all possible solutions propagating in such structures. The nonlinearity in this method is treated in an approximated manner in which only the transverse component is used in the Kerr-nonlinearity term. In addition, we must assume that the nonlinear refractive index change is small compared to the linear one. The second model is based on the finite element method, in which the electromagnetic field components are computed numerically. In this method, the nonlinearity is treated correctly and all the electric field

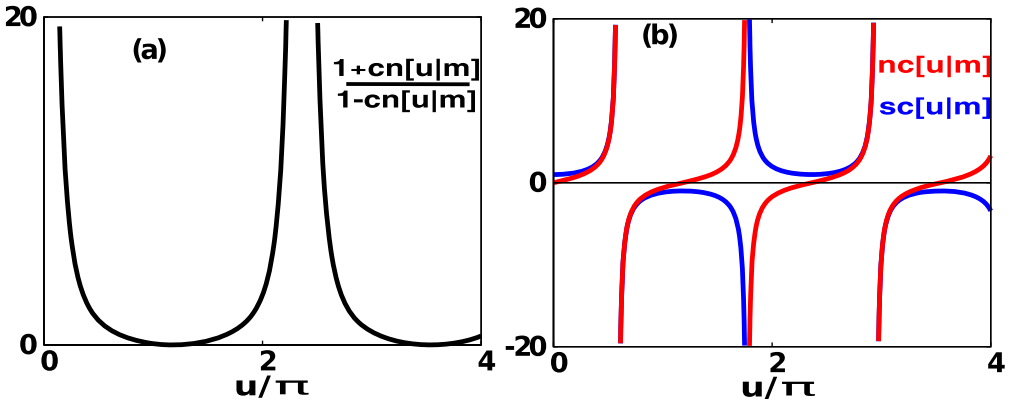


**Figure A1.** Unbounded periodic Jacobi elliptical functions with argument $u$ and parameter $m = 0.5$. The global shape of the functions does not change $\forall\, m \in [0, 1]$.

components are used in the Kerr nonlinearity without any further assumptions. Finally, we presented several numerical results to validate our models and illustrate their limitations. We have found that the methods provide identical results at low powers, while at high power there exist some discrepancies between them due to the assumptions required by the semi-analytical model. This semi-analytical approach EJEM gives more insights into the behaviour of the nonlinear dispersion curves and field profiles than the more numerical FEM approach, while the FEM approach describes the nonlinearity in a proper way, the only disadvantage being that the field profiles are computed numerically. We have also demonstrated the influence of the linear and nonlinear anisotropic terms of the permittivity on the nonlinear dispersion curves and on the field profiles for two different cases defined in the frame of the first model. First, for $a_{\mathrm{nl}}^{\mathrm{EJEM}} < 0$, we have found that the nonlinear metamaterial core with positive Kerr-type nonlinearity can act as a defocusing medium. Second, for $a_{\mathrm{nl}}^{\mathrm{EJEM}} > 0$, we have presented one interesting example providing a huge enhancement of the nonlinearity; moreover, losses decrease with power unlike in the usual isotropic plasmonic slot waveguides. Using nonlinear FDTD simulations, we have also shown the stability of the main symmetric mode up to intermediate powers, for several anisotropic configurations, including one with a strong elliptical anisotropy.

## Acknowledgments

G R would like to thank the PhD school ED 352 'Physique et Sciences de Matière' and the International Relation Service of Aix-Marseille University (projectAAP 2015 'Noliplasmo 2D') for their funding.

## Appendix A. Unbounded solutions in the EJEM

In this appendix, we briefly describe the unbounded solutions obtained in the case $a_{\mathrm{nl}}^{\mathrm{EJEM}} < 0$ presented in section 3.1.1. We have mentioned before that the only bounded solution with finite electromagnetic energy in the nonlinear core for $a_{\mathrm{nl}}^{\mathrm{EJEM}} < 0$ can be obtained when $q_{\mathrm{core}}^2 < 0$ (see equation (5)) and $C_0 > 0$ (see equation (10)) under the condition shown in equation (11).

In this appendix, we will study the other possible subcases in the frame of $a_{\mathrm{nl}}^{\mathrm{EJEM}} < 0$. First, we begin with the subcase in which the condition shown in equation (11) is not satisfied. Since we are only looking for a real solution for equation (12), we can write the nonlinear wave equation as

$$\frac{dH_y}{\sqrt{\gamma^4 - \delta^2 H_y^2 + H_y^4}} = \pm\sqrt{\frac{1}{A}}\,dx, \tag{A.1}$$

where $\gamma^4 = AC_0$ and $\delta^2 = AQ$. The coefficients $\gamma^4 > 0$ and $\delta^2 > 0$ since $A$, $Q$, and $C_0$ are positive quantities in this subcase (see section 3.1.1). Integrating equation (A.1) and using the relation 263.00 from [34] yields the magnetic field profile in the nonlinear core

$$H_y^2(x) = \gamma^2 \frac{1 + \mathrm{cn}\{\,\}}{1 - \mathrm{cn}\{\,\}},$$
$$\mathrm{cn}\{\,\} = \mathrm{cn}\left[\mp 2\gamma\sqrt{\frac{1}{A}}\left(x + \frac{d_{\mathrm{core}}}{2}\right) + X_0 \,\middle|\, m\right], \tag{A.2}$$

where

$$m = \frac{2\gamma^2 + \delta}{4\gamma^2}, \quad X_0 = \mathrm{cn}^{-1}\left[\frac{H_{\mathrm{left}}^2 - \gamma^2}{H_{\mathrm{left}}^2 + \gamma^2} \,\middle|\, m\right]. \tag{A.3}$$

This solution represents the magnetic field component in the nonlinear core for $a_{\mathrm{nl}}^{\mathrm{EJEM}} < 0$, $q_{\mathrm{core}}^2 < 0$, and $C_0 > 0$ when the condition equation (11) is not satisfied, which means that $q_{\mathrm{core}}^4 < 2C_0|a_{\mathrm{nl}}^{\mathrm{EJEM}}|/k_0^2$. This kind of solution is described by periodic and unbounded functions (see figure A1(a)) such that the electromagnetic energy in the core is infinite. A similar unbounded solution has already been obtained in nonlinear dielectric waveguides [38].

Next, we consider the other subcases in which we get unbounded solutions for $a_{\mathrm{nl}}^{\mathrm{EJEM}} < 0$. Table A1 shows their unbounded magnetic field profiles with their reduced parameters according to the signs of $q_{\mathrm{core}}^2$ and $C_0$. The first two

**Table A1.** Unbounded magnetic field profiles with their reduced parameters for the case $a_{\mathrm{nl}}^{\mathrm{EJEM}} < 0$. The reduced parameter $A = 2/(k_0^2|a_{\mathrm{nl}}^{\mathrm{EJEM}}|)$ is fixed for all the cases, while $Q = k_0^2|q_{\mathrm{core}}^2|$ for $q_{\mathrm{core}}^2 < 0$ and $Q = k_0^2 q_{\mathrm{core}}^2$ for $q_{\mathrm{core}}^2 > 0$.

| $q_{\mathrm{core}}^2$ | $C_0$ | $\gamma^2$ | $\delta^2$ | m | $X_0$ | $H_y(x)$ |
|---|---|---|---|---|---|---|
| $<0$ | $<0$ | $\frac{-AQ+\sqrt{(AQ)^2+4A\mid C_0\mid}}{2}$ | $\frac{+AQ+\sqrt{(AQ)^2+4A\mid C_0\mid}}{2}$ | $\frac{\gamma^2}{\gamma^2+\delta^2}$ | $\mathrm{nc}^{-1}\left[\frac{H_{\mathrm{left}}}{\delta}\middle\vert m\right]$ | $\delta\mathrm{nc}\left[\pm\sqrt{\frac{\gamma^2+\delta^2}{A}}\left(x+\frac{d_{\mathrm{core}}}{2}\right)+X_0\middle\vert m\right]$ |
| $>0$ | $>0$ | $\frac{AQ+\sqrt{(AQ)^2-4AC_0}}{2}$ | $\frac{AQ-\sqrt{(AQ)^2-4AC_0}}{2}$ | $\frac{\gamma^2-\delta^2}{\gamma^2}$ | $\mathrm{sc}^{-1}\left[\frac{H_{\mathrm{left}}}{\delta}\middle\vert m\right]$ | $\delta\mathrm{sc}\left[\pm\sqrt{\frac{\gamma^2+\delta^2}{A}}\left(x+\frac{d_{\mathrm{core}}}{2}\right)+X_0\middle\vert m\right]$ |
| $>0$ | $<0$ | $\frac{AQ+\sqrt{(AQ)^2+4A\mid C_0\mid}}{2}$ | $\frac{-AQ+\sqrt{(AQ)^2+4A\mid C_0\mid}}{2}$ | $\frac{\gamma^2}{\gamma^2+\delta^2}$ | $\mathrm{nc}^{-1}\left[\frac{H_{\mathrm{left}}}{\delta}\middle\vert m\right]$ | $\delta\mathrm{nc}\left[\pm\sqrt{\frac{\gamma^2+\delta^2}{A}}\left(x+\frac{d_{\mathrm{core}}}{2}\right)+X_0\middle\vert m\right]$ |

columns of table A1 give the signs of $q_{\mathrm{core}}^2$ and $C_0$, and the last column represents the corresponding magnetic field profiles in terms of one of the unbounded Jacobi elliptical functions nc $[u|m]$ or sc $[u|m]$ [42, 43] with argument $u$ and parameter $m$ (see also figure A1(b)). The other columns correspond to the reduced parameters used to describe the magnetic field profiles shown in the last column. We have used the same procedure to derive the nonlinear magnetic field profiles as in sections 3.1.1, 3.1.2 and [15, 20]. One can see that the first and the third subcases can be described by the same unbounded function nc$[u|m]$; however, the reduced parameters $\gamma^2$ and $\delta^2$ are reversed. In our study, we will exclude the solutions depicted in table A1 since we are looking for a guided nonlinear wave propagating with finite energy in the core.

## Appendix B. Adapted FEM to match EJEM assumptions

In this appendix, we show that the FEM presented in section 3.2 can be compared to the semi-analytical approach described in section 3.1 by taking into account all the EJEM assumptions. In the frame of the EJEM, the nonlinearity depends only on the transverse component of the electric field $E_x$, and the nonlinear refractive index change is small compared to the linear one. Therefore, one way to tackle this problem is to consider only the weak formulation for the full (TM) wave equation in terms of the magnetic field forcing both the inhomogeneous permittivity term induced by the nonlinearity and the structure interfaces to take into account the EJEM assumptions

$$\begin{aligned}\frac{-1}{k_0^2}\int_\Gamma \frac{1}{\epsilon_{zz}(x)}\frac{\mathrm{d}h_y}{\mathrm{d}x}\frac{\mathrm{d}h_y'}{\mathrm{d}x}\mathrm{d}x + \int_\Gamma h_y(x)h_y'(x)\mathrm{d}x \\ - n_{\mathrm{eff}}^2\int_\Gamma \frac{1}{\epsilon_{xx}(x)}h_y(x)h_y'(x)\mathrm{d}x \\ - \int_\Gamma \frac{|E_x|^2}{\epsilon_{xx}^2\epsilon_{zz}}(n_{\mathrm{eff}}^2(\alpha_{zz}\epsilon_{xx} - \alpha_{xx}\epsilon_{zz}) \\ - \alpha_{zz}\epsilon_{xx}^2)h_y(x)h_y'(x)\mathrm{d}x = 0, \end{aligned} \tag{B.1}$$

such that $\forall h_y'(x) \in \mathrm{H}_0^1(\gamma)$. We look for $h_y(x) \in \mathrm{H}_0^1(\gamma)$, where $\mathrm{H}_0^1(\gamma)$ is the Sobolev space of order 1 with null Dirichlet boundary conditions on the domain of integration $\Gamma$. Equation (B.1) is derived from the first equation in system (31), taking into account the two EJEM assumptions. Consequently, unlike system (31), only the linear part of the permittivity components $\epsilon_{xx}$ and $\epsilon_{zz}$ (see equation (1)) appear in equation (B.1). The nonlinearity is represented by the fourth term in which the nonlinear parameters $\alpha_{xx}$ and $\alpha_{zz}$ are non-zero only in the core. Equation (B.1) and the first equation in system (31) are identical in the linear regime. The algorithm used to solve equation (B.1) is quite similar to algorithm 1: we start by an initial field $E_x^{\mathrm{init}}$ in the fourth term of equation (B.1) and compute the eigenvector $h_y$ with the corresponding eigenvalue $n_{\mathrm{eff}}$ for the chosen mode. The rescaling factor $\chi$ is computed at each iteration for a given fixed power $P_{\mathrm{tot}}$. Using the longitudinal $z$ component of the pointing vector integrated over the transverse $x$-direction, and equation (2$a$) with only the linear part of the permittivity $\epsilon_{xx}$, we can compute the rescaling factor $\chi$ for a given $P_{\mathrm{tot}}$ in the frame of the EJEM assumptions as

$$P_{\mathrm{tot}} = \frac{\Re e(n_{\mathrm{eff}})\chi^2}{2\epsilon_0 c}\int_\Gamma \frac{|h_y(x)|^2}{\epsilon_{xx}}\mathrm{d}x, \tag{B.2}$$

where the rescaled eigenvector $H_y = \chi h_y$ will be used with the eigenvalue $n_{\mathrm{eff}}$ to compute $E_x$ (using equation (2$a$) with only the linear part of the permittivity $\epsilon_{xx}$ in the denominator), which will be used as an input in the fourth term of equation (B.1) for the next iteration.

Finally, we would like to mention that the single-component eigenvalue problem shown in equation (B.1) or in [8], in the frame of our FEM formalism using the fixed power algorithm, cannot be solved taking into account all the electric field components in the Kerr-type nonlinearity. To clarify this point, we consider the longitudinal $z$ component of the pointing vector integrated over the transverse $x$-direction without the EJEM assumptions:

$$P_{\mathrm{tot}} = \frac{\Re e(n_{\mathrm{eff}})}{2\epsilon_0 c}\int_\Gamma \frac{\chi^2}{\epsilon_{xx} + \alpha_{xx}(|E_x|^2 + |E_z|^2)}|h_y(x)|^2\mathrm{d}x. \tag{B.3}$$

In order to obtain the rescaling factor $\chi$, we need to express $E_x$, $E_z$ in the previous formula in terms of the eigenvector $h_y$ and $\chi$, which is not possible since both $E_x$ and $E_z$ depend on the nonlinear permittivity $\epsilon_x$ and $\epsilon_z$, respectively, as is shown in equations (2). Another way to solve this problem is to write the weak formulation in terms of the electric field components $E_x$ and $E_z$ only, as it is then possible to obtain an explicit formula for $\chi$ as a function of $P_{\mathrm{tot}}$. However, this approach requires the use of discontinuous Galerkin method in the

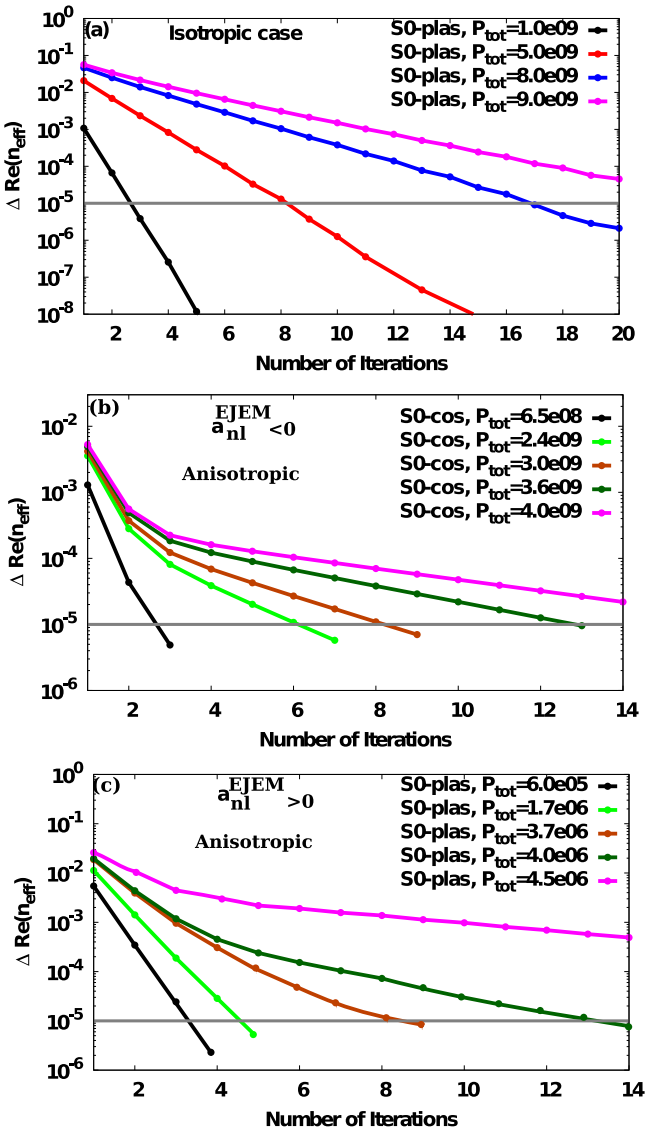


**Figure C1.** Convergence of the full NL FEM for the nonlinear fundamental symmetric mode (a) in the isotropic case and (b) and (c) in the anisotropic case for $a_{\mathrm{nl}}^{\mathrm{EJEM}} < 0$ and $a_{\mathrm{nl}}^{\mathrm{EJEM}} > 0$, respectively. The gray horizontal line represents the tolerance, which is set to be $10^{-5}$.

FEM [72, 73] since $E_x$ is a discontinuous function, which is beyond the scope of the present study. Consequently, in order to take into account all the electric field components in the Kerr nonlinearity in our FEM using the fixed power algorithm, we must solve the coupled eigenvalue problem in terms of the continuous electromagnetic field components $E_z$ and $H_y$ as described in section 3.2.

## Appendix C. Convergence of the FEM method

In this appendix, we discuss the convergence of the full NL FEM presented in section 3.2. In figure C1, we study the convergence of the FEM method for the three different cases presented in section 4 using the same parameters. We only show the results for the fundamental nonlinear symmetric mode in each case (the results for the other modes are similar). Here, $\Delta\Re e(n_{\mathrm{eff}}) = |\Re e(n_{\mathrm{eff}}^{i}) - \Re e(n_{\mathrm{eff}}^{i-1})|/|\Re e(n_{\mathrm{eff}}^{i})| \quad \forall\, i \in [1, N]$, where $\Re e(n_{\mathrm{eff}}^{i})$ is the real part of the eigenvalue for the step $i$ and N is the step number in the procedure. We set our tolerance at $10^{-5}$ such that, for each power value, the convergence is achieved if the following criterion is satisfied: $\Delta\Re e(n_{\mathrm{eff}}) < 10^{-5}$. As can be seen in figure C1, we need few steps to reach the convergence at low powers, while, at very high powers, the number of iterations increases until we reach power values in which the algorithm does not converge within the number of iterations we fixed (20 for the isotropic and 14 for the anisotropic case); these power values are represented by the pink curves in figure C1. The reason for this is, above these power values, the nonlinear dispersion curves start to have a negative slope (see figures 2–4 for the fundamental symmetric modes), which means that we will have two values for the effective index at the same power. However, in the frame of the fixed power algorithm, for a given input power, we look for the corresponding effective index of the investigated nonlinear mode (see section 3.2). This means that the FEM based on the fixed power algorithm fails to follow the branches of the nonlinear dispersion curves with a negative slope, which usually corresponds to unstable modes. The current versions of the FEM based on the fixed power algorithm converge only to possibly stable modes [45, 58].

## References

[1] Tien P K 1971 *Appl. Opt.* **10** 2395–413
[2] Stegeman G I and Seaton C T 1985 *J. Appl. Phys.* **58** R57–78
[3] Stegeman G, Wright E M, Finlayson N, Zanoni R and Seaton C 1988 *J. Lightwave Technol.* **6** 953–70
[4] Kauranen M and Zayats A V 2012 *Nat. Photon.* **6** 737–48
[5] Rukhlenko I D, Premaratne M and Agrawal G P 2011 *Opt. Express* **19** 206–17
[6] Ariyasu J, Seaton C T, Stegeman G I, Maradudin A A and Wallis R F 1985 *J. Appl. Phys.* **58** 2460–6
[7] Agranovich V, Babichenko V and Chernyak V Y 1980 *Sov. Phys. JETP Lett.* **32** 512
[8] Agranovich V M, Babichenko V S and Chernyak V Y 2014 *Phys. Rev.* A **89** 023816
[9] Ajith R and Mathew V 2015 *Opt. Commun.* **346** 183–7
[10] Feigenbaum E and Orenstein M 2007 *Opt. Lett.* **32** 674–6
[11] Davoyan A R, Shadrivov I V and Kivshar Y S 2008 *Opt. Express* **16** 21209–14
[12] Rukhlenko I D, Pannipitiya A, Premaratne M and Agrawal G P 2011 *Phys. Rev.* B **84** 113409
[13] Ferrando A, Milián C and Skryabin D V 2013 *J. Opt. Soc. Am.* B **30** 2507–22
[14] Salgueiro J R and Kivshar Y S 2014 *J. Opt.* **16** 114007
[15] Walasik W, Renversez G and Ye F 2016 *Phys. Rev.* A **93** 013826
[16] Davoyan A R, Shadrivov I V and Kivshar Y S 2009 *Opt. Express* **17** 20063–8
[17] Salgueiro J R and Kivshar Y S 2010 *Appl. Phys. Lett.* **97** 081106
[18] Nozhat N and Granpayeh N 2012 *Opt. Commun.* **285** 1555–9
[19] Rukhlenko I D, Pannipitiya A and Premaratne M 2011 *Opt. Lett.* **36** 3374–6
[20] Walasik W and Renversez G 2016 *Phys. Rev.* A **93** 013825
[21] Elsawy M M R and Renversez G 2016 *Opt. Lett.* **41** 1542–4

[22] Elsawy M M, Nazabal V, Chauvet M and Renversez G 2016 Improved nonlinear plasmonic slot waveguide: a full study *Proc. SPIE* **9884** 98840J
[23] Ciattoni A, Rizza C and Palange E 2010 *Phys. Rev.* A **81** 043839
[24] Campione S, de Ceglia D, Vincenti M A, Scalora M and Capolino F 2013 *Phys. Rev.* B **87** 035120
[25] Ciattoni A, Rizza C, Marini A, Falco A D, Faccio D and Scalora M 2016 *Laser Photon. Rev.* **10** 517–25
[26] Neira A D, Olivier N, Nasir M E, Dickson W, Wurtz G A and Zayats A V 2015 *Nat. Commun.* **6** 7757
[27] Alam M Z, De Leon I and Boyd R W 2016 *Science* **352** 795–7
[28] Capretti A, Wang Y, Engheta N and Negro L D 2015 *Opt. Lett.* **40** 1500–3
[29] Elsawy M M R and Renversez G 2017 *J. Opt.* **19** 075001
[30] Ishii S, Shalaginov M Y, Babicheva V E, Boltasseva A and Kildishev A V 2014 *Opt. Lett.* **39** 4663–6
[31] Avrutsky I, Salakhutdinov I, Elser J and Podolskiy V 2007 *Phys. Rev.* B **75** 241402
[32] Rukhlenko I D, Premaratne M and Agrawal G P 2012 *Nanotechnology* **23** 444006
[33] Abramowitz M 1974 *Handbook of Mathematical Functions, With Formulas, Graphs, and Mathematical Tables* (New York: Dover)
[34] Paul F and Byrd M D F 1971 *Handbook of Elliptic Integrals for Engineers and Scientists* (Berlin: Springer)
[35] Byrd P F and Friedman M D 1985 *J. Appl. Phys.* **58** 2453–9
[36] Drouart F, Renversez G, Nicolet A and Geuzaine C 2008 *J. Opt. A: Pure Appl. Opt.* **10** 125101
[37] Davoyan A R, Shadrivov I V and Kivshar Y S 2009 *Opt. Express* **17** 21732–7
[38] Chen W and Maradudin A A 1988 *J. Opt. Soc. Am.* B **5** 529–38
[39] Rizza C, Ciattoni A and Palange E 2011 *Phys. Rev.* A **83** 053805
[40] Stegeman G I and Seaton C T 1984 *Opt. Lett.* **9** 235–7
[41] Mihalache D, Stegeman G I, Boardman A, Twardowski T, Seaton C, Wright E and Zanoni R 1987 *Opt. Lett.* **12** 187–9
[42] Salas A 2014 *Appl. Math. Sci.* **8** 8781–9
[43] Von Seggern D H 2006 *Standard Curves and Surfaces with Mathematica* 2nd edn (Boca Raton, FL: Chapman & Hall)
[44] Rahman B M A, Souza J R and Davies J B 1990 *IEEE Photon. Tech. Lett.* **2** 265–7
[45] Li Q, Sammut R and Pask C 1992 *Opt. Commun.* **94** 37–43
[46] Polstyanko S V and Lee J F 1996 *R. Sci.* **31** 913–22
[47] Désévédavy F, Renversez G, Troles J, Brilland L, Houizot P, Coulombier Q, Smektala F, Traynor N and Adam J L 2009 *Appl. Opt.* **48** 3860–5
[48] Zolla F, Renversez G, Nicolet A, Kuhlmey B, Guenneau S, Felbacq D, Argyros A and Leon-Saval S 2012 *Foundations of Photonic Crystal Fibres* 2nd ed (London: Imperial College Press)
[49] Ferrando A, Zacarés M, de Córdoba P F, Binosi D and Monsoriu J A 2003 *Opt. Express* **11** 452–9
[50] Dular P, Geuzaine C, Henrotte F and Legros W 1998 *IEEE Trans. Magn.* **34** 3395–8
[51] Geuzaine C 2007 *Proc. Appl. Math. Mech.* **7** 1010603–4
[52] Geuzaine C and Remacle J F 2009 *Int. J. Numer. Methods Eng.* **79** 1309–31
[53] Ciattoni A, Rizza C and Palange E 2011 *Phys. Rev.* A **83** 043813
[54] Olivier M *et al* 2014 *Opt. Mater. Express* **4** 525–40
[55] Boyd R W 2008 *Nonlinear Optics* (New York: Academic Press)
[56] Palik E D 1998 *Handbook of Optical Constants of Solids* Vol 3 (Burlington, MA: Academic Press)
[57] Akhmediev N N and Ankiewicz A 1997 *Solitons: Nonlinear Pulses and Beams* (London: Chapman & Hall)
[58] Rahman B A, Fernandez F A and Davies J B 1991 *Proc. IEEE* **79** 1442–8
[59] Johnson P B and Christy R W 1972 *Phys. Rev.* B **6** 4370–9
[60] Nazabal V, Starecki F, Doualan J L, Němec P, Camy P, Lhermite H, Bodiou L, Anne M, Charrier J and Adam J 2016 *Opt. Mater.* **58** 390–7
[61] Yan K, Vu K, Wang R and Madden S 2016 *Opt. Express* **24** 23304–13
[62] Argyropoulos C, Estakhri N M, Monticone F and Alù A 2013 *Opt. Express* **21** 15037–47
[63] Savelev R S, Shadrivov I V, Belov P A, Rosanov N N, Fedorov S V, Sukhorukov A A and Kivshar Y S 2013 *Phys. Rev.* B **87** 115139
[64] Rizza C, Di Falco A and Ciattoni A 2011 *Appl. Phys. Lett.* **99** 221107
[65] Grandidier J, des Francs G C, Massenot S, Bouhelier A, Markey L, Weeber J C, Finot C and Dereux A 2009 *Nano Lett.* **9** 2935–9
[66] Smalley J S T, Vallini F, Kanté B and Fainman Y 2014 *Opt. Express* **22** 21088–105
[67] Javani M H and Stockman M I 2016 *Phys. Rev. Lett.* **117** 107404
[68] Ciattoni A, Marinelli R, Rizza C and Palange E 2013 *Appl. Phys.* B **110** 23–6
[69] Rodriguez A, Soljacic M, Joannopoulos J D and Johnson S G 2007 *Opt. Express* **15** 7303–18
[70] Oskooi A F, Roundy D, Ibanescu M, Bermel P, Joannopoulos J D and Johnson S G 2010 *Comp. Phys. Commun.* **181** 687–702
[71] Taflove A 2013 *Advances in FDTD Computational Electrodynamics* (Boston, MA: Artech House)
[72] Dolean V, Fol H, Lanteri S and Perrussel R 2008 *J. Comput. Appl. Math.* **218** 435–45
[73] El Bouajaji M and Lanteri S 2013 *Appl. Math. Comput.* **219** 7241–51